Transient-Absorption Pump-Probe Spectra as Information-Rich Observables: Case Study of Fulvene

Zhaofa Li , Jiawei Peng , Yifei Zhu , Chao Xu , Maxim F. Gelin * , Feng Long Gu * , Zhenggang Lan *

Posted Date: 18 February 2025

doi: 10.20944/preprints202502.1269.v1

Keywords: Conical Intersections; Transient Absorption Pump-Probe Spectroscopy; Symmetrical Quasi-Classical/Meyer-Miller-Stock-Thoss; Doorway Window Approximation

 doi:10.20944/preprints202502.1269.v1

Article

Transient-Absorption Pump-Probe Spectra as Information-Rich Observables: Case Study of Fulvene

Zhaofa Li [1,2], Jiawei Peng [2], Yifei Zhu [2], Chao Xu [2], Maxim F. Gelin [3,*], Feng Long Gu [2,*] and Zhenggang Lan [2,*]

[1] School of Chemistry, South China Normal University, Guangzhou 510006, P. R. China
[2] MOE Key Laboratory of Environmental Theoretical Chemistry, SCNU Environmental Research Institute, Guangdong Provincial Key Laboratory of Chemical Pollution and Environmental Safety, School of Environment, South China Normal University, Guangzhou 510006, P. R. China
[3] School of Science, Hangzhou Dianzi University, Hangzhou 310018, China
* Correspondence: maxim@hdu.edu.cn (M.F.G.); gu@scnu.edu.cn (F.L.G.); zhenggang.lan@m.scnu.edu.cn (Z.L.)

Abstract: Conical intersections (CIs) are the most efficient channels of photodeactivation and energy transfer, while femtosecond spectroscopy is the main experimental tool delivering information on molecular CI-driven photoinduced processes. In this work, we undertake comprehensive ab initio investigation of the CI-mediated internal conversion in fulvene by simulating evolutions of electronic populations, bond lengths and angles, and time-resolved transient absorption (TA) pump-probe (PP) spectra. TA PP spectra are evaluated on-the-fly, by combining the symmetrical quasi-classical/Meyer-Miller-Stock-Thoss (SQC/MMST) dynamics and the doorway-window representation of spectroscopic signals. We show that the simulated time-resolved TA PP spectra reveal not only the population dynamics but also the key nuclear motions as well as mode-mode couplings. We also demonstrate that TA PP signals are not only experimental observables: They can also be considered as information-rich purely theoretical observables, which deliver more information on the CI-driven dynamics than conventional electronic populations. This information can be extracted by the appropriate theoretical analyses of time-resolved TA PP signals.

Keywords: conical intersections; transient absorption pump-probe spectroscopy; symmetrical quasi-classical/meyer-miller-stock-thoss; doorway window approximation

1. Introduction

Nonadiabatic processes taking place near crossing areas of potential energy surfaces (PESs) are ubiquitous in photochemistry and photobiology [1–6]. When two electronic states have the same multiplicity, conical intersections (CIs), i.e. degeneracy areas between adjacent adiabatic PESs, facilitate radiationless transitions [7] and population transfer [8]. CI-driven nonadiabatic processes occur, usually, on the femtosecond timescale [3,8]. It is thus instrumental but challenging to determine microscopic mechanisms and molecular motions governing the CI-driven wavepacket dynamics.

Nowadays, femtosecond spectroscopy is the main experimental source of information on ultrafast photoinduced processes [9–17], and transient-absorption (TA) pump-probe (PP) spectroscopy is one of the most widespread techniques [18–24]. TA PP spectroscopy delivers information on the wavepacket dynamics in the (coupled) ground and lower-lying excited electronic states. The information is encoded into, e.g., integral TA-PP spectra $I_{int}(\tau, \omega_{pr})$ [25] which are monitored as a function of the time time delay between the pump and probe pulses (so-called population time τ) and probe frequency ω_{pr}, but depend implicitly on the excitation frequency ω_{pu}, durations of the PP pulses, and parameters describing molecular system under study. However, it is impossible to comprehensively characterize photoinduced dynamics at CIs by using TA PP spectra alone: theoretical support is essential for their interpretation. Thus, simulation of time-resolved spectra is important because it helps us to extract the essential information on nonadiabatic dynamics near CIs[26–30]. Consequently, considerable

 doi:10.20944/preprints202502.1269.v1

efforts were devoted to simulate nonlinear time-resolved signals within the framework of quantum dynamics[31,32], hierarchical equations of motion (HEOM)[33], mixed quantum-classical Liouville equations[34,35], surface hopping[36–39], and Ehrenfest dynamics[40]. These efforts were aimed to build a more straightforward connection between nonadiabatic dynamics driven by CIs and time-resolved signals[25,41–48].

With the advancement of computational facilities and theoretical algorithms, efforts of many groups have been shifted to the construction of on-the-fly protocols for simulations of spectroscopic signals for realistic molecular systems [45,48–57]. These efforts open the possibility to microscopically understand ultrafast time-resolved spectra of polyatomic systems and to get insight into nonadiabatic dynamics involving large-amplitude molecular motions.

Usually, the on-the-fly simulations are conducted within the trajectory-based dynamics formulism. Among them, the quasiclassical or semiclassical dynamics methods based on the mapping Hamiltonian [58–60] received considerable attentions. Different versions of the mapping approach were implemented to study nonadiabatic dynamics at CIs in recent decades[61–72]. Within the mapping framework, different theoretical approaches were proposed to simulate different types of nonlinear spectroscopic signals [73–89]. It is to be noted that the direct simulation of spectroscopic third-order response functions by the mapping approaches is quite tedious even for model systems [46]. On the other hand, the direct inclusion of laser fields at different time delays in the propagation is also computationally costly [90–93]. In simple words, more rigorous methods generally have to face larger computational costs. It is thus worthwhile to invoke some alternative, practical ideas for the simulation of time-resolved spectra[48].

The doorway-window (DW) approximation[94–98] accounting for finite duration and arbitrary spectral shapes of the pump and probe pulses provides a practical approach for the evaluation of spectroscopic signals. This approximation can conveniently be interfaced with any ab initio trajectory method: As the input, the DW protocol requires exclusively electronic energies and transition dipole moments (TDMs) along trajectories. So far, the ab initio DW methodology has been combined with two commonly used simulation techniques: surface-hopping (Tully's fewest switches [99–101], Landau-Zenner [102,103], and machine-learning-enhanced Landau-Zenner [104]) and Ehrenfest [105].

Recently, a combination of symmetrical quasi-classical/Meyer-Miller-Stock-Thoss (SQC/MMST) dynamics with the DW approximation has been proposed for the simulation of TA PP signals [106]. Clearly, the SQC/MMST approach permits one to calculate nonadiabatic wavepacket dynamics with (usually) sufficient accuracy and at affordable computational costs [84,107–112]. Furthermore, the mapping approach may have advantages over the surface hopping and Ehrenfest counterparts in reproducing electronic coherences [64,113], which can become essential for adequate simulation of TA PP and other nonlinear spectroscopic signals. In addition, the mapping approach can be reformulated in the adiabatic representation [114] and conveniently used in the on-the-fly simulations to describe realistic molecular systems [114–117].

In this work, we took a practical idea to simulate TA PP signals by ab initio methods by interfacing the DW approximation and the SQC/MMST dynamics (DW-SQC/MMST). It has both theoretical and methodological dimensions. On the methodological side, we further extend the application base of the on-the-fly DW simulation protocol [102].

On the theoretical side, we explore the possibility of abstracting the key information about the nuclear motions involved in the CI-driven nonadiabatic dynamics by combined on-the-fly simulation of the traditional dynamical observables (electronic populations, bond lengths, and bond angles) and TA PP spectra.

The molecule of fulvene was chosen as a typical CI-driven molecular system, which is frequently used as a real-world representative of "Tully's third model" [118]. The photoinduced dynamics in fulvene is fairly well understood at the ab initio level [119,119–128]. This allows us to concentrate on squeezing additional information from the TA PP signals. It essential that surface hopping methods do not give very precise description of fulvene's population dynamics [119–122], while the SQC/MMST

 doi:10.20944/preprints202502.1269.v1

method with triangular window function provides results which are consistent with ab initio multiple spawning (AIMS) data [122]. This lends support to the choosing of the SQC/MMST method for simulations of TA PP signals of fulvene. Our results show that the TA PP signals directly reflect the key molecular motions in the nonadiabatic dynamics of fulvene. This work thus provides useful ideas on how to connect ultrafast spectroscopic signals with the essential features in nonadiabatic dynamics.

2. Theoretical Methods and Computational Details

2.1. SQC/MMST Approach

Mapping models, in which an F-level quantum system is mapped to a system with F coupled continuous degrees of freedom (DoFs), provide practical ideas for the construction of classical-like dynamics approaches for the simulation of quantum evolutions of realistic large system[64,67]. In the MMST model[58–60], a set of discrete quantum states is mapped to a group of coupled classical oscillators. With the SQC protocol, the initial sampling and the final assignment of the electronic DoFs is performed through the symmetrical triangle window function [129,130]. More rigorous derivations can be found in the previous works [59,110,131,132]. By combining the MMST mapping model with the SQC protocols, the SQC/MMST approach allows us to simulate the nonadiabatic dynamics [107,108] with acceptable accuracy and affordable computational costs[109,111,112]. Since the SQC/MMST method is easy to reformulate in the adiabatic representation,[114] it can be conveniently combined with the ab into quantum chemistry software to describe the nonadiabatic dynamics in realistic molecular systems[115–117] by using the trajectory-adjusted zero-point energy (ZPE) correction γ [114,133].

The classical MMST Hamiltonian in the adiabatic representation reads

$$H = \frac{1}{2\mathbf{M}}\mathbf{P}_{kin}^2 + \sum_i^F \left[\frac{1}{2}(x_i)^2 + \frac{1}{2}(p_i)^2 - \gamma\right] V_i(\mathbf{R}). \tag{1}$$

Here the kinematic momentum $\mathbf{P}_{kin}$ is defined as

$$\mathbf{P}_{kin} = \mathbf{P} + \sum_{ij}^F (x_i p_j)\mathbf{d}_{ij}(\mathbf{R}) \tag{2}$$

where $\mathbf{R}$ and $\mathbf{P}$ are nuclear coordinates and momenta; x_i and p_i are coordinates and momenta of the mapped electronic states $i = 1, ..., F$; F is the total number of these states; $V_i(\mathbf{R})$ is the potential energy of the electronic state i; $\mathbf{d}_{ij}$ is the first-order non-adiabatic coupling vector.

The effective potential

$$V_{\text{eff}}(\mathbf{R})) = \sum_i^F \frac{1}{2}(x_i^2 + p_i^2 - 2\gamma)V_i(\mathbf{R}) \tag{3}$$

is customarily rearranged into the symmetrized form

$$V_{\text{eff}}(\mathbf{R})) = \frac{1}{F}\sum_i^F V_i(\mathbf{R}) + \frac{1}{F}\sum_{ij}^F \frac{1}{4}(x_i^2 + p_i^2 - x_j^2 - p_j^2)(V_i(\mathbf{R}) - V_j(\mathbf{R})), \tag{4}$$

which enhances numerical stability.

 doi:10.20944/preprints202502.1269.v1

The classical equations of motion generated by the Hamiltonian of Eq. (1) assume the form [114]:

$$\begin{aligned}
\dot{x}_i &= p_i \frac{1}{F}\sum_j^F (V_i(\mathbf{R}) - V_j(\mathbf{R})) + \sum_j^F (x_j \mathbf{d}_{ji}(\mathbf{R})) \cdot \frac{\mathbf{P}_{kin}}{\mathbf{M}} \\
\dot{p}_i &= -x_i \frac{1}{F}\sum_j^F (V_i(\mathbf{R}) - V_j(\mathbf{R})) + \sum_j^F (p_j \mathbf{d}_{ji}(\mathbf{R})) \cdot \frac{\mathbf{P}_{kin}}{\mathbf{M}} \\
\dot{\mathbf{R}} &= \frac{\mathbf{P}_{kin}}{\mathbf{M}} \\
\dot{\mathbf{P}}_{kin} &= -\frac{\partial V_{\text{eff}}(\mathbf{R})}{\partial \mathbf{R}} + \frac{1}{2}\sum_{ij}^F (p_i p_j + x_i x_j)(V_j(\mathbf{R}) - V_i(\mathbf{R}))\mathbf{d}_{ji}(\mathbf{R}).
\end{aligned} \tag{5}$$

In the SQC/MMST simulations, the window function (which should not be confused with the window function of the DW representation) is employed for the initial sampling and final assignment of discrete electronic states [108,129]. The so-called triangle window function is defined as [130]

$$W_i(\mathbf{n} = n_1, ...n_i, ...n_f) = w_1(n_i) \prod_{i \neq j}^F w_0(n_i, n_j), \tag{6}$$

where

$$w_1(n_i) = \begin{cases} (2 - \gamma - n_i)^{2-F} & \text{for} \quad 1 - \gamma < n_i < 2 - \gamma \\ 0 & \text{otherwise} \end{cases} \tag{7}$$

and

$$w_0(n_i, n_j) = \begin{cases} 1 & \text{for} \quad n_j < 2 - 2\gamma - n_i \\ 0 & \text{otherwise} \end{cases} \tag{8}$$

In other words, $w_i = 1$ if the system is in the state i, and $w_i = 0$ otherwise.

The action-angle sampling method produces initial electronic positions and momenta

$$\begin{aligned}
x_i^0 &= \sqrt{2(n_i^0 + \gamma)} \cos\theta, \\
p_i^0 &= \sqrt{2(n_i^0 + \gamma)} \sin\theta,
\end{aligned} \tag{9}$$

where n_i^0 is obtained by using the triangle window function and $\theta \in [-\pi, \pi]$. For the final assignment, the triangle window function recasts the action variables n_i into integers 0 or 1,

$$n_i = \frac{1}{2}(x_i)^2 + \frac{1}{2}(p_i)^2 - \gamma. \tag{10}$$

Recently, Miller and Cotton proposed a trajectory-adjusted ZPE scheme, wherein each trajectory incorporates its specific ZPE correction γ[134]. Once the electronic coordinates and momenta are initially sampled, the ZPE correction is defined as

$$\gamma_i = \frac{1}{2}(x_i^0)^2 + \frac{1}{2}(p_i^0)^2 - \delta_{ij}, \tag{11}$$

where j is the adiabatic electronic state in the initial sampling. Naturally, the value for γ_i varies for each trajectory. Using this trajectory-specific γ_i, the action variable of the electronic DoF is defined as

$$n_i = \frac{1}{2}(x_i)^2 + \frac{1}{2}(p_i)^2 - \gamma_i \tag{12}$$

during the trajectory propagation [134].

 doi:10.20944/preprints202502.1269.v1

Meanwhile, the MMST Hamiltonian in the adiabatic representation is expressed in terms of the trajectory-adjusted γ_i as follows:

$$H = \frac{1}{2\boldsymbol{M}}\boldsymbol{P}_{kin}^2 + \sum_i^F \left[\frac{1}{2}(x_i)^2 + \frac{1}{2}(p_i)^2 - \gamma_i\right] E_i(\boldsymbol{R}). \tag{13}$$

More details on the trajectory-adjusted ZPE approach can be found in Ref. [134]. Recently, further interpretations and physical insights into the adjustable ZPE correction γ were presented[66,110,132, 135,136].

2.2. DW Representation of TA PP Signals

The integral TA PP signal $I_{int}(\tau, \omega_{pr})$ can be obtained as a sum of non-rephasing (α = NR, $\xi_\alpha = 1$) and rephasing (α = R, $\xi_\alpha = -1$) terms, each of which consists of the ground-state bleach (GSB), stimulated emission (SE), and excited-state absorption (ESA) contributions. $I_{int}(\tau, \omega_{pr})$ can be evaluated in terms of the third-order response functions $R_{\alpha k}(t_3, t_2, t_1)$ as follows [25,42,47,48]:

$$I_{int}(\tau, \omega_{pr}) \sim \mathrm{Re} \sum_{\alpha=\mathrm{R,\,NR}} \sum_{k=0,\mathrm{I,II}} \int_{-\infty}^{\infty} dt \int_0^{\infty} dt_3 \int_0^{\infty} dt_2 \int_0^{\infty} dt_1 \times \tag{14}$$

$$E_{pu}(t+\tau-t_3-t_2-t_1)E_{pu}(t+\tau-t_3-t_2)E_{pr}(t-t_3)E_{pr}(t)e^{i\xi_\alpha\omega_{pu}t_1}e^{i\omega_{pr}t_3}R_{\alpha k}(t_3,t_2,t_1).$$

Here $k = 0$, I, II correspond to the GSB, SE, and ESA contributions, $E_j(t)$ and ω_j are the dimensionless envelopes of the pump ($j = pu$) and probe ($j = pr$) pulses, and τ is the time delay between them.

To evaluate the response functions $R_{\alpha k}(t_3, t_2, t_1)$, it is convenient to subdivide all molecular electronic states into three manifolds 0, I and II which correspond to the ground, lower-lying, and upper-lying states. Then the molecular Hamiltonian of Eq. (1) assumes the block-diagonal form,

$$H = \begin{pmatrix} H_0 & H_{0\mathrm{I}} & 0 \\ H_{\mathrm{I}0} & H_{\mathrm{I}} & 0 \\ 0 & 0 & H_{\mathrm{II}} \end{pmatrix}. \tag{15}$$

Here the Hamiltonians H_0, H_{I} and H_{II} – each of which can be represented as a sum of kinetic and potential parts – describe the (nonadiabatic) dynamic in the corresponding manifolds. $H_{0\mathrm{I}} = H_{\mathrm{I}0}^\dagger$ are the inter-manifold coupling terms, which are relevant to the nonadiabatic couplings in the adiabatic representation. The rising and lowering TDM operators can also be recast in the block-diagonal form

$$\mu^\uparrow = \begin{pmatrix} 0 & \mu_{0,\mathrm{I}} & 0 \\ 0 & 0 & \mu_{\mathrm{I,II}} \\ 0 & 0 & 0 \end{pmatrix}, \quad \mu^\downarrow = \begin{pmatrix} 0 & 0 & 0 \\ \mu_{\mathrm{I},0} & 0 & 0 \\ 0 & \mu_{\mathrm{II,I}} & 0 \end{pmatrix}. \tag{16}$$

As explained in Refs. [100,102], the TA PP signal of Eq. (14) can be represented in the form suitable for on-the-fly simulations by performing a series of approximations. First, the quantum DW approximation is applied, according to which

(i) The pump and probe pulses are well temporally separated. Hence the time delay τ between the pulses is (much) longer than the pump (τ_{pu}) and probe (τ_{pr}) pulse durations.

(ii) The pump and probe pulses are short on the nuclear dynamics timescale.

With these assumptions, the integral TA PP signal takes the DW form [100,102]

$$I_{int}(\tau, \omega_{pr}) = \omega_{pr}\mathrm{Tr}\Big[D(\omega_{pu})\Big(e^{iH_0\tau}W_0(\omega_{pr})e^{-iH_0\tau} + e^{iH_{\mathrm{I}}\tau}(W_{\mathrm{I}}(\omega_{pr}) - W_{\mathrm{II}}(\omega_{pr}))e^{-iH_{\mathrm{I}}\tau}\Big)\Big], \tag{17}$$

where

$$D(\omega_{pu}) = \int_{-\infty}^{\infty} dt_2' \int_0^{\infty} dt_1 E_{pu}(t_2')E_{pu}(t_2'-t_1)e^{i\omega_{pu}t_1}e^{-iH_{\mathrm{I}}t_1}\mu_{\mathrm{I},0}\rho_0 e^{iH_0t_1}\mu_{0,\mathrm{I}} + h.c. \tag{18}$$

Preprints.org (www.preprints.org) | NOT PEER-REVIEWED | Posted: 18 February 2025 doi:10.20944/preprints202502.1269.v1

is the doorway operator, ρ_0 is the initial nuclear distribution in manifold 0, which is determined by either the thermal equilibrium or a particular vibrational level, and

$$\begin{aligned} W_0(\omega_{pr}) &= \int_{-\infty}^{\infty} dt' \int_0^{\infty} dt_3 E_{pr}(t') E_{pr}(t'+t_3) e^{i\omega_{pr}t_3} e^{iH_0 t_3} \mu_{0,\mathrm{I}} e^{-iH_\mathrm{I} t_3} \mu_{\mathrm{I},0} + h.c. \\ W_\mathrm{I}(\omega_{pr}) &= \int_{-\infty}^{\infty} dt' \int_0^{\infty} dt_3 E_{pr}(t') E_{pr}(t'+t_3) e^{i\omega_{pr}t_3} \mu_{\mathrm{I},0} e^{iH_0 t_3} \mu_{0,\mathrm{I}} e^{-iH_\mathrm{I} t_3} + h.c. \\ W_\mathrm{II}(\omega_{pr}) &= \int_{-\infty}^{\infty} dt' \int_0^{\infty} dt_3 E_{pr}(t') E_{pr}(t'+t_3) e^{i\omega_{pr}t_3} \mu_{\mathrm{I,II}} e^{-iH_\mathrm{II} t_3} \mu_{\mathrm{II,I}} e^{iH_\mathrm{I} t_3} + h.c. \end{aligned} \tag{19}$$

are the window operators.

Then, a series of classical DW approximations is applied.

(iii) The DW operators $D(\omega_{pu})$ and $W_k(\omega_{pr})$ become functions of the nuclear coordinates $\boldsymbol{R}$ and momenta $\boldsymbol{P}$, $D(\omega_{pu}, \boldsymbol{R}, \boldsymbol{P})$ and $W_k(\omega_{pr}, \boldsymbol{R}, \boldsymbol{P})$.

(iv) Radiative transitions are treated within the classical Condon approximation [74,137].

(v) The initial vibrational distribution ρ_0 in the doorway function (18) is replaced by the Wigner distribution $\rho_g^{Wig}(\boldsymbol{R}, \boldsymbol{P})$ [138].

(vi) The trace Tr[...] in Eq. (17) is evaluated by Monte Carlo averaging $\langle ... \rangle$ over classical initial conditions.

(vii) The Heisenberg propagators in Eq. (17) are replaced by the evolution along (quasi) classical trajectories $\boldsymbol{R}(T)$, $\boldsymbol{P}(T)$.

For converting these approximations into operational expressions and simulation protocols, we denote: electronic states in manifolds 0, I, II as $|g\rangle$, $|e\rangle$, $|f\rangle$; potential energy functions in these states as $V_g(\boldsymbol{R})$, $V_e(\boldsymbol{R})$, $V_f(\boldsymbol{R})$; transition frequencies as $U_{eg}(\boldsymbol{R}) = V_e(\boldsymbol{R}) - V_g(\boldsymbol{R})$ and $U_{fe}(\boldsymbol{R}) = V_f(\boldsymbol{R}) - V_e(\boldsymbol{R})$; matrix elements of TDMs as $\mu_{ge}(\boldsymbol{R}) = \langle g|\mu_{0,\mathrm{I}}|e\rangle$ and $\mu_{fe}(\boldsymbol{R}) = \langle f|\mu_{\mathrm{II,I}}|e\rangle$. Then approximations (iii) and (iv) yield [74,137]

$$\langle g|e^{iH_0 t_3} \mu_{0,\mathrm{I}} e^{-iH_\mathrm{I} t_3}|e\rangle \approx e^{iU_{ge}(\boldsymbol{R})t_3} \mu_{ge}(\boldsymbol{R}), \tag{20}$$

$$\langle f|e^{iH_\mathrm{II} t_3} \mu_{\mathrm{II,I}} e^{-iH_\mathrm{I} t_3}|e\rangle \approx e^{iU_{fe}(\boldsymbol{R})t_3} \mu_{fe}(\boldsymbol{R}) \tag{21}$$

and we arrive at the final quasiclassical DW expression for the integral TA PP signal:

$$\begin{aligned} I_{int}(\tau, \omega_{pr}) &= I_{int}^{GSB}(\tau, \omega_{pr}) + I_{int}^{SE}(\tau, \omega_{pr}) + I_{int}^{ESA}(\tau, \omega_{pr}), \\ I_{int}^{GSB}(\tau, \omega_{pr}) &= \omega_{pr} \sum_e \int d\mathbf{R}_g d\mathbf{P}_g D(\omega_{pu}, \mathbf{R}_g, \mathbf{P}_g) W_0(\omega_{pu}, \mathbf{R}_g(\tau), \mathbf{P}_g(\tau)), \\ I_{int}^{SE}(\tau, \omega_{pr}) &= \omega_{pr} \sum_e \int d\mathbf{R}_g d\mathbf{P}_g D(\omega_{pu}, \mathbf{R}_g, \mathbf{P}_g) W_\mathrm{I}(\omega_{pu}, \mathbf{R}_e(\tau), \mathbf{P}_e(\tau)), \\ I_{int}^{ESA}(\tau, \omega_{pr}) &= -\omega_{pr} \sum_e \int d\mathbf{R}_g d\mathbf{P}_g D(\omega_{pu}, \mathbf{R}_g, \mathbf{P}_g) W_\mathrm{II}(\omega_{pu}, \mathbf{R}_e(\tau), \mathbf{P}_e(\tau)). \end{aligned} \tag{22}$$

Here $\mathbf{R}_g$ and $\mathbf{P}_g$ represent the initial nuclear coordinates and momenta in the electronic ground state sampled according to the Wigner distribution $\rho_g^{Wig}(\mathbf{R}_g, \mathbf{P}_g)$, $\mathbf{R}_g(\tau)$ and $\mathbf{P}_g(\tau)$ denote the nuclear coordinates and momenta propagated in the electronic ground state up to $t = \tau$, and $\mathbf{R}_e(\tau)$ and $\mathbf{P}_e(\tau)$ denote the nuclear coordinates and momenta propagated up to $t = \tau$ in manifold I of the lower-lying excited electronic states. The quasiclassical doorway function reads

$$D(\omega_{pu}, \mathbf{R}_g, \mathbf{P}_g) = |\mu_{ge}(\mathbf{R}_g)|^2 E_{pu}^2(\omega_{pu} - U_{eg}(\mathbf{R}_g)) \rho_g^{Wig}(\mathbf{R}_g, \mathbf{P}_g), \tag{23}$$

 doi:10.20944/preprints202502.1269.v1

and the quasiclassical window functions are defined as

$$\begin{aligned} W_0(\omega_{pu}, \mathbf{R}_g(\tau), \mathbf{P}_g(\tau)) &= \sum_e |\mu_{ge}(\mathbf{R}_g(\tau))|^2 E_{pr}^2(\omega_{pr} - U_{eg}(\mathbf{R}_g(\tau))), \\ W_{\mathrm{I}}(\omega_{pu}, \mathbf{R}_e(\tau), \mathbf{P}_e(\tau)) &= |\mu_{ge(\tau)}(\mathbf{R}_e(\tau))|^2 E_{pr}^2(\omega_{pr} - U_{e(\tau)g}(\mathbf{R}_e(\tau))), \\ W_{\mathrm{II}}(\omega_{pu}, \mathbf{R}_e(\tau), \mathbf{P}_e(\tau)) &= \sum_f |\mu_{e(\tau)f}(\mathbf{R}_e(\tau))|^2 E_{pr}^2(\omega_{pr} - U_{fe(\tau)}(\mathbf{R}_e(\tau))). \end{aligned} \tag{24}$$

Here $E_{pu}(\omega)$ and $E_{pr}(\omega)$ are the Fourier transforms of $E_{pu}(t)$ and $E_{pr}(t)$, and the notion $e(\tau)$ means that a trajectory initiated in an excited state e may jump into another electronic state.

The above derivations have been made under the assumption that nonadiabatic coupling operators $H_{0\mathrm{I}} = H_{\mathrm{I}0}^{\dagger}$ can be neglected on the timescale of interest. Once the internal conversion $e(\tau) \to g$ is allowed, Eq. (17) remains valid, but the window functions W_k defined per Eq. (24) have to be replaced by the new window functions $\overline{W}_k$ which are defined in terms of the original window functions as follows [100]:

$$\overline{W}_0 = W_0, \tag{25}$$

$$\overline{W}_{\mathrm{I}} = \begin{bmatrix} W_{\mathrm{I}}, & \text{if trajectory stays within I} \\ -W_0, & \text{if trajectory jumps from I to 0,} \end{bmatrix} \tag{26}$$

$$\overline{W}_{\mathrm{II}} = \begin{bmatrix} W_{\mathrm{II}}, & \text{if trajectory stays within I} \\ 0, & \text{if trajectory jumps from I to 0.} \end{bmatrix} \tag{27}$$

If a trajectory jumps from manifold I back to the ground state, then $e(\tau)$ changes to g in Eq. (26). Owing to the $e(\tau) \to g$ internal conversion, two GSB contributions arise: the cold and the hot. The cold contribution is the conventional GSB signal which reveals the nuclear wavepacket on the electronic ground state. It is described by the window function W_0 of Eq. (25). The hot contribution is the internal-conversion-induced GSB signal, that reveals the manifold-I trajectory which jumps to the electronic ground state after the $e(\tau) \to g$ internal conversion. This trajectory contributes to the GSB signal with a minus sign, $-W_0$ in Eq. (26) [100]. In the SQC/MMST simulations, the DW functions are straightforwardly calculated by "binning" trajectories to the windows corresponding to the currently occupied electronic states [130].

2.3. Computational Details

The optimized structures of fulvene are shown in Figure 1. The S_0 minimum was optimized at the B3LYP/6-31G(d) level by using the Gaussian 16 package [139]. In the SQC/MMST simulations, two state-averaged CASSCF(6,6) method with the basis set 6-31G(d) was employed in the MOLPRO2022 package [140]. Initial nuclear coordinates and momenta were sampled according to the Wigner distribution of the lowest vibrational level on the ground electronic state[141]. Initial sampling and final assignments of electronic states were performed by using the symmetrical triangle window function of Eq. (6), while coordinates and momenta of mapping electronic degrees of freedom were generated according to the action-angle distribution of Eq. (9). The time steps were fixed at 0.2 fs and 0.002 fs for nuclear and mapping electronic motions, respectively. All dynamics calculations were carried out with the JADE package [116,141].

 doi:10.20944/preprints202502.1269.v1

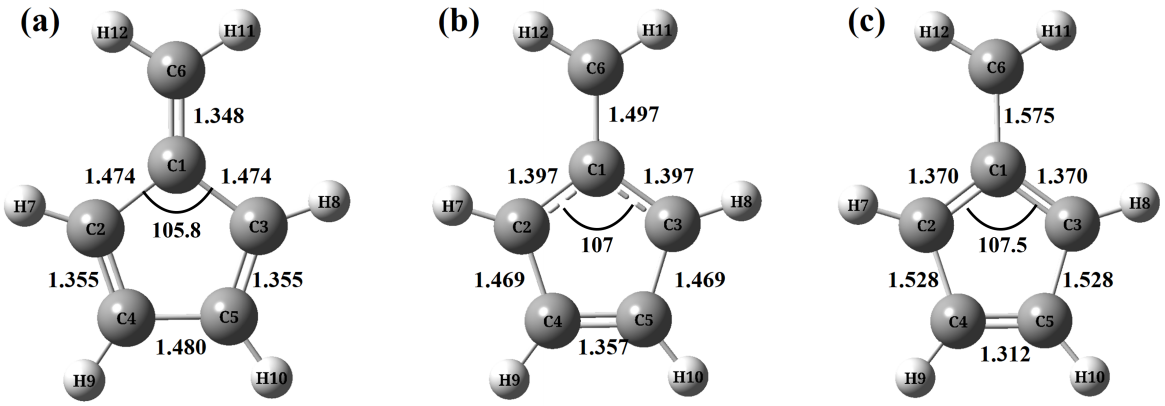

Figure 1. Optimized equilibrium structures of fulvene in (a) S_0, (b) S_1 and (c) CI.

For fulvene, manifold I contains a single state S_1, while manifold II consists of four states S_2-S_5. 100 trajectories were initiated on the S_1 state and propagated for 600 fs in manifold I to simulate the hot GSB, SE, and ESA signals. Another 100 trajectories were initiated on the S_0 state and propagated for 600 fs to simulate the cold GSB signal. To evaluate ESA signals, snapshots from every trajectory were taken to obtain vertical excitation energies and TDMs for the states of manifold II.

Gaussian pump and probe pulses were chosen, $E_a(t) = \exp\{-(t/\tau_a)^2\}$ and $E_a(\omega) = \exp\{-(\omega\tau_a)^2/4\}$, with $\tau_a = 2$ fs. This gives the pulse bandwidth of 1.04 eV (full width at half maximum).

3. Results and Discussion

To setup the stage, we begin with the populations of the S_0 and S_1 states of fulvene which are shown in Figure 2. These populations correlate with those obtained by the numerically accurate AIMS method [119–122] as well as with those computed by the SQC/MMST method [122]. No decay of the S_1 population occurs within the first 5 fs, during which the wavepacket travels from the Franck-Condon to the CI region. Then, the S_1 population decreases rapidly, reaching half of its initial value at 9 fs and less than 20% within 10-15 fs. After that, a weak-amplitude population recurrence occurs within 15-25 fs. This flat recurrence is caused by the torsional motions which bring the wavepacket back to the PES crossing each 20-25 fs. After the recurrence, the S_1 population remains small, but its quenching slows down considerably.

 doi:10.20944/preprints202502.1269.v1

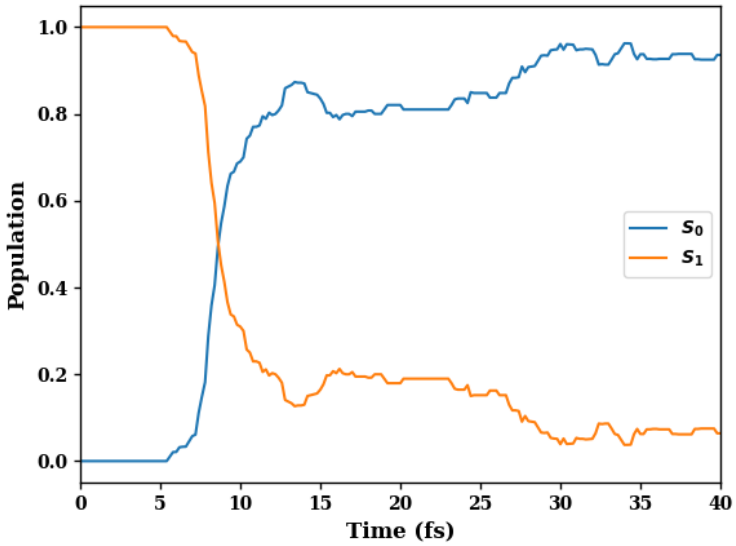

Figure 2. Time-dependent populations of the S_0 and S_1 states of fulvene.

Panels (a, b, c) of Figure 3 show the SE, ESA, GSB contributions to the integral TA PP spectrum, while panel (d) displays the total TA PP spectrum. The spectra are initiated with the pump pulse with $\omega_{pu} = 4.39$ eV, which is in resonance with the $S_0 - S_1$ transition (see Table A1). Note that all observables of the present section are evaluated at the SA6-CASSSCF level. The SE signals obtained at the SA2-CASSCF level are given in Appendix A. These two levels of the electronic structure theory give very similar results. The long-time TA PP spectra are also shown in the Appendix A.

At $\tau = 0$, the SE spectrum is concentrated around ω_{pu}, as expected. Within the first 10 fs, it rapidly moves to the red. This redshift is accompanied by the significant loss of intensity. Then $I_{int}^{SE}(\tau, \omega_{pr})$ exhibits a pronounced recurrence around $\tau \approx 25$ fs, but the overall intensity of the spectrum after 10 fs is roughly an order of magnitude lower than the initial intensity. This behavior correlates with the S_1 population evolution in Figure 2. However, the S_1 population recurrence tells us nothing about the details of the wavepacket motion on S_1. The SE signal, on the contrary, demonstrates that a fraction of the wavepacket returns almost to the initial position in the Franck-Condon region. This indicates that the SE signal can be used as an informative observable containing more information than the traditional excited-state population. Note that the low-intensity high-amplitude oscillations in $I_{int}^{SE}(\tau, \omega_{pr})$ last for several hundreds of femtoseconds (see Appendix A), indicating a partially reversible wavepacket motion at the CI. This kind of behavior is highly unusual for CI systems, which normally exhibit irreversible ultrafast population transfer [1,2].

The ESA contribution is shown in Figure 3 (b). At short times, $I_{int}^{ESA}(\tau, \omega_{pr})$ has two components: the upper high-intensity component starting at $\omega_{pr} \approx 4.2$ eV and the lower low-intensity component starting at $\omega_{pr} \approx 2$ eV. These two branches of the ESA spectrum reveal the $S_1 - S_4/S_5$ and the $S_1 - S_2$ transitions, respectively (see Appendix A). Initially, both ESA components move to the higher energy domain and reach their maxima around 10 fs. Then the intensity of the upper component decreases rapidly, exhibits a minimum around 20 fs, and continues oscillatory evolution at longer times. The lower component vanishes after 10 fs on the intensity scale of the figure. Both SE and ESA signals reflect the same wavepacket motion on the S_1 state. They differ in the "spectator states" (manifold 0 for SE and manifold II for ESA) which are used for the detection of the signals. It is not surprising therefore that the SE and ESA signals behave similarly. More precisely, the spectra in panels (a) and (b) look like mirror images of each other: while the SE spectrum moves to the red, reaches a minimum, exhibits a maximum and keeps in oscillating at much lower intensity, the ESA spectrum moves to the blue, reaches a maximum, exhibits a minimum and keeps in oscillating at much lower intensity.

 doi:10.20944/preprints202502.1269.v1

This mirror behavior indicates that the energy gap between the states contributing to the SE (ESA) spectrum initially decreases (increases) with τ.

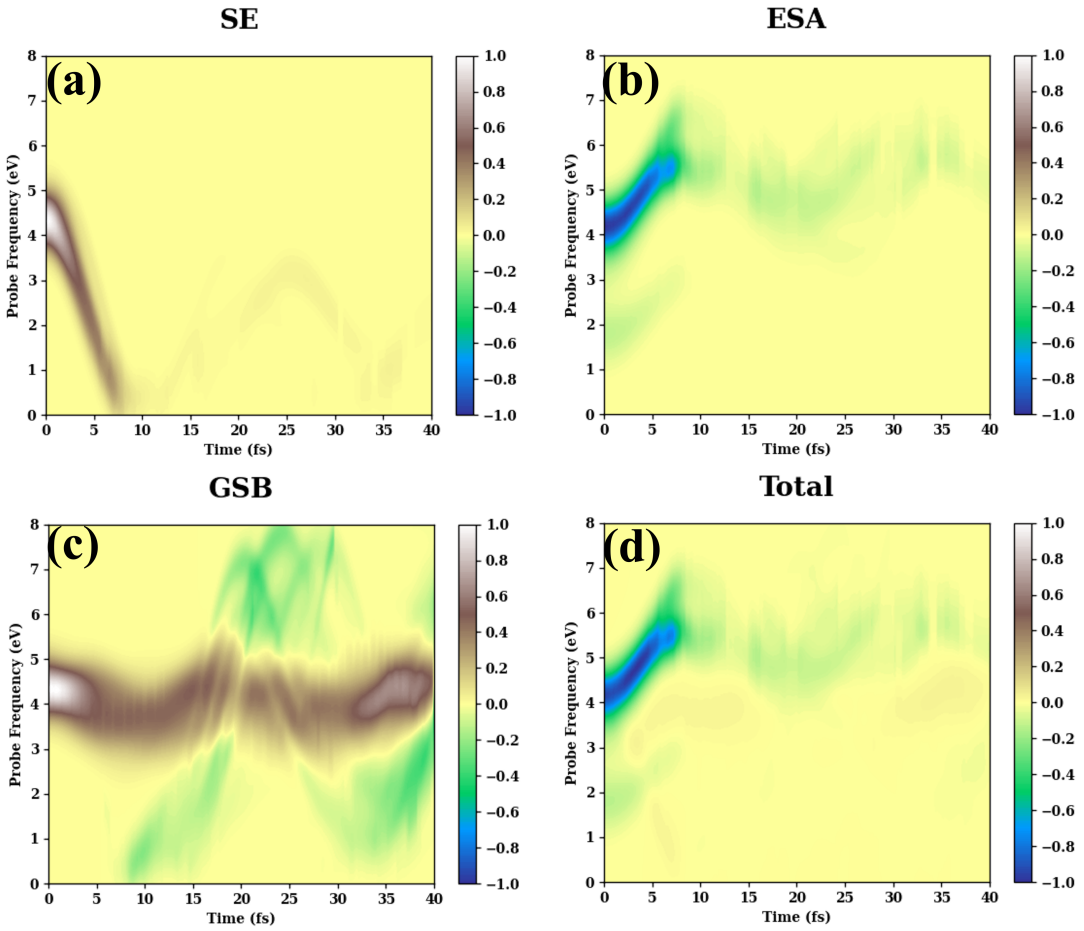

Figure 3. Normalized SE (a), ESA (b), GSB (c) and total (d) integral TA PP spectra of fulvene vs pump-probe delay τ and the probe carrier frequency ω_{pr}. The carrier frequency of the pump pulse, $\omega_{pu} = 4.39$ eV, is in resonance with the S_1 state.

Figure 3 (c) shows the GSB signal which is composed of the cold (positive) and hot (negative) components. The cold spectrum exhibits undamped oscillations with a $\sim$ 2 eV amplitude, $\sim$ 20 fs period, and $\sim$ 4 eV baseline. The spectrum is dominated by the $S_0 - S_1$ transitions in the Franck-Condon region (see Appendix A). The hot spectrum emerges at $\sim$ 10 fs (that correlates with the initial decay of the S_1 population in Figure 2) and shows high-amplitude ($\sim$ 7 eV) oscillations with a period of $\sim$ 20 fs around the baseline of $\sim$ 4 eV. Such a large oscillation amplitude of the hot spectrum is caused by the excess kinetic energy acquired by the wavepacket in the course of its CI-driven internal conversion. The same baseline of 4 eV is a signature of the dominant role of the $S_0 - S_1$ transitions in the formation of both cold and hot signals. Similar oscillation periods of the cold and hot components seem to be a remarkable feature of fulvene, caused by the fact that various nuclear motions in this molecule have similar periods around 20 fs.

The total TA PP signal is shown in Figure 3 (d). It is dominated by the ESA contribution. This is a consequence of the large values of TDMs to higher-lying excited states of manifold II.

The above discussions clearly show the close correspondence between the TA PP signals in Figure 3 and the population dynamics in Figure 2. However, it is even more important to ask whether it is possible to establish correlation between the spectral patterns in the TA PP signals and the key molecular motions in the nonadiabatic dynamics. For this purpose, several critical structures in the nonadiabatic dynamics were optimized at the SA2-CASSCF(6,6)/6-31G(d) level, as shown in Figure 1.

 doi:10.20944/preprints202502.1269.v1

The S_0 equilibrium in Figure 1(a) shows an exocyclic bond with a single bond double bond alternation. For the S_1 equilibrium (b), however, the alternation is reversed and reveals a biradical character[127]. The $S_0 - S_1$ CI (c) is similar to the S_1 minimum, which implies that the quick nonadiabatic decay may easily take place after the initial vibrational relaxation to the S_1 minimum [127]. Importantly, the C1-C6 bond distance is the leading coordinate affecting the CI-driven internal conversion and TA PP spectra. Figure 1 shows clearly that C1-C6, C2-C4, and C3-C5 bond distances are longer near the CI region than those at the S_0 and S_1 minima. On the other hand, C1-C2 and C1-C3 bond distances are shorter in the vicinity of the CI region, but longer near the Frank-Condon region. In addition, the C2-C1-C3 angle is smaller at the S_1 and S_0 equilibrium and larger near the $S_0 - S_1$ CI. Hence, extension of the bonds C2-C4 and C3-C5, contraction of the bonds C1-C2 and C1-C3, and decrease of the angle C2-C1-C3 accompany the wavepacket motion from the Frank-Condon region toward the CI region (see Figure 1). These skeleton motions finally comprise the symmetric tuning modes governing the CI-driven internal conversion.

The linear-interpolated reaction pathways between the optimized S_0 minimum and S_0/S_1 CI and the relevant TDMs obtained by the single point calculations at both SA2-CASSCF(6,6)/6-31G(d) and SA6-CASSCF(6,6)/6-31G(d) levels are presented in Figure 4. Both levels of electronic structure theory give very similar results for potential energy profiles and TDMs. It is thus safe to use any of them for the simulation of spectroscopic signals. This is corroborated by the comparison of Figure 3 and its counterpart in the Appendix A.

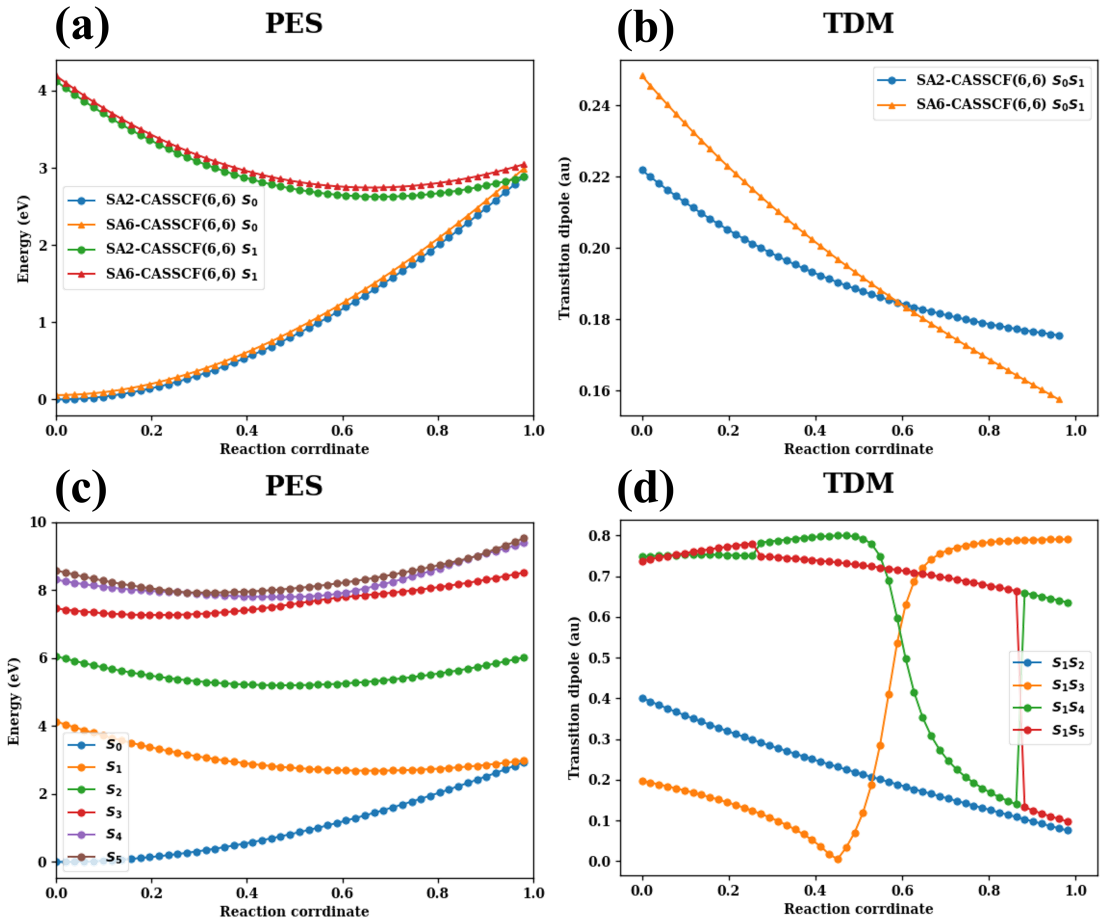

Figure 4. (a) Linear interpolated PESs of S_0 and S_1 between S_0 minimum and S_0/S_1 CI obtained at SA2-CASSCF(6,6)/6-31G(d) and SA6-CASSCF(6,6)/6-31G(d) levels. (b) Linear interpolated TDMs from S_0 to S_1 between S_0 minimum and S_0/S_1 CI obtained at SA2-CASSCF(6,6)/6-31G(d) and SA6-CASSCF(6,6)/6-31G(d) levels. (c) Linear interpolated PESs from S_0 to S_5 between S_0 minimum and S_0/S_1 CI. (d) Linear interpolated TDMs from S_1 to $S_2 - S_5$ between S_0 minimum and S_0/S_1 CI.

 doi:10.20944/preprints202502.1269.v1

Along the interpolated pathways that are driven by the above reactive coordinates and shown in Figure 4 (a) and (c), no barrier exists between the Franck-Condon region and the CI seam. In the Franck-Condon region, a large gradient is observed. Clearly, there is a S_1 minimum in the pathway toward the CI, and this minimum lies lower than the CI. As a result, the so-called sloped CI is created [127].

The $S_0 - S_1$ TDM decreases along the reaction pathways (Figure 4 (b)). Among electronic transitions from the S_1 state to higher-lying states (Figure 4 (d)), $S_1 - S_4$ and $S_1 - S_5$ TDMs are larger than the $S_0 - S_1$ TDM at the Franck-Condon region (Figure 4 (b)). This explains why the ESA signals are stronger than the SE signals. Interestingly, an abrupt rise of $S_1 - S_3$ TDM is related to the S_3/S_4 surface crossing, while the exchange of the TDM values between $S_1 - S_4$ and $S_1 - S_5$ transitions is due to the S_4/S_5 PES crossing (shown in Figure 4 (d)).

Ab initio simulations permit one to explore how the time evolution of TA PP signals is correlated with the dynamics of specific molecular bond lengths and angles. The results are presented in Figure 5. Panel (a) shows how the C1-C6 bond distance evolves in time on the S_1 (a) and S_0 (e) states. In the first 10 fs, elongation of the C1-C6 bond is observed. When the C1-C6 distance reaches 1.5-1.7 Å, some trajectories jump back to the ground state, as is clear from Figures 5 (a) and (e). The C1-C6 bond displays pronounced oscillations on the S_1 state. Starting from 7-10 fs, a large-amplitude stretching motion of the C1-C6 bond emerges also on the ground state. Evolutions of the bond distances in panels (b), (c), (f) and (g) on the S_1 state also exhibit qualitatively similar behaviors. Panels (d) and (h) display evolutions of the bond angle C2-C1-C3 on the excited and ground electronic states, respectively. In panel (d), the C2-C1-C3 angle increases during the first 10 fs. When the angle reaches 110°-120°, only a few trajectories remain on S_1. Afterwards, the remaining trajectories produce high-amplitude oscillations of the C2-C1-C3 angle. There are no trajectories on the S_0 state before 10 fs (panel (h)). At ≈ 10 fs, abundant ground-state trajectories emerge for the C2-C1-C3 angles around 110°-120°. At longer times, a large amplitude of the C2-C1-C3 bending was observed. Note that the evolution of the C2-C1-C3 angle (panels (d) and (h)) is synchronous with the C1-C6 stretching motion (panels (a) and (e)). Such unusually fast bending motion can be explained by the fact that the C1-C6 stretching motion and the C2-C1-C3 bending motion are strongly coupled with each other since both involve the C1 atom. In contrast, other motions (e.g., the C4-C5 stretching, see Appendix A) are only weakly involved in the dynamic propagation, as they either show small oscillation amplitudes or different oscillation periods.

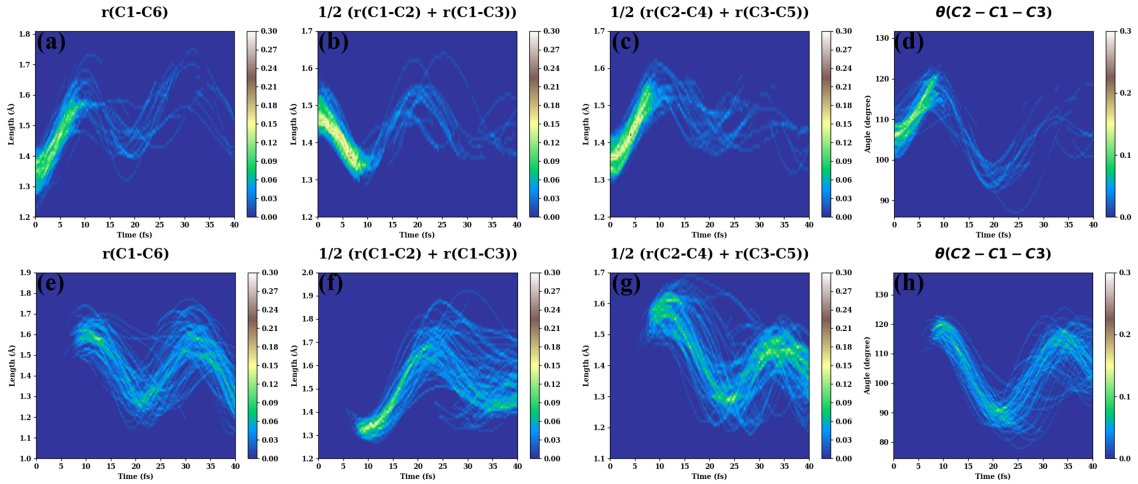

Figure 5. Normalized time-dependent distributions of C1-C6 bond lengths (a, e), C1-C2 and C1-C3 symmetric stretches (b, f), C2-C4 and C3-C5 symmetric stretches (c, g), and C2-C1-C3 bendings (d, h). The upper panels are evaluated for the first excited state S_1, while the lower panels are evaluated for S_0.

Interestingly, the nuclear motions on S_0 are more erratic than those on S_1. This is manifested in a larger spread of trajectories in the lower panels in comparison with that in the upper panels. The

 doi:10.20944/preprints202502.1269.v1

reason is that internal conversion produces large-amplitude wavepackets which experience vibrational energy redistribution induced by the mode-mode couplings.

By the combination of the above discussions, the relationship between the population dynamics, the key molecular motions, and the TA PP signals is well established. As the carrier frequency of the pump pulse is resonant with the $S_0 - S_1$ transition, the nonadiabatic dynamics of fulvene start from the first excited state. In the Franck-Condon region, the large gradient of the S_1 state drives ultrafast nuclear motions, leading to pronounced stretching (C1-C6, C1-C2/C1-C3, C2-C4/C3-C5) and bending (C2-C1-C3) motions. Following these motions, the system first arrives in the S_1 minimum and then moves close to the CI on the excited state. This motion also leads to the TDM decrease (Figure 4). As a consequence, the SE signal moves to the low-frequency domain quickly, which is consistent with the time scale of the aforementioned nuclear motions along the internal coordinates. In addition, all trajectories follow similar propagation patterns and no dispersion is observed. Thus the SE signal does not show bifurcation in the early stage of the dynamics. Similar patterns were observed in the ESA signal. The only difference is that the ESA signal moves to the higher energy domain because energy gaps between the S_1 state and the higher-lying excited electronic states responsible for the relevant transitions increase with time.

When the CI is reached, many trajectories jump back to the ground state, resulting in significant population transfer. Hence, both the SE and ESA signals suddenly become weaker at $\sim 7 - 10$ fs, which directly reflects the ultrafast nonadiabatic transitions. After that, a few trajectories stay on the excited state for a rather long time. As the S_1 minimum is lower than the CI and the shape of the CI is sloped, these trajectories oscillate near the S_1 minimum. Due to the lack of dissipation, these oscillations endure for quite a long time and induce the oscillatory patterns in the weak SE and ESA signals (see Appendix A). Whenever the trajectories access the CI, there is a minor fluctuation of the electronic population due to the nonadiabatic transition, which is consistent with the population dynamics in Figure 2. As some trajectories jump back to the ground state, they create the GSB hot signal. Here, the molecular vibrations are highly excited by the excessive energy emerged after internal conversion. This leads to diversity in the trajectory propagation patterns and results in quite erratic hot GSB signals. Due to the small system size and lack of dissipation, these signals show large-amplitude oscillations, and their periods are consistent with the vibrational periods of the few key coordinates, such as the C1-C6 stretching motion. At the same time, the mode-mode coupling is also responsible for spreading of trajectories, producing a broad hot GSB signal. Overall, the TA PP signals provide clear fingerprints which allow us to monitor the population decay and identify the key tuning modes in the nonadiabatic dynamics.

In addition, evolutions of the asymmetric stretching modes are given in the Appendix A. The modes exhibit oscillations with a ~ 20 fs period and different initial phases. As a result, these modes produce characteristic pulsating wavepacket, which is symmetric with respect to positive and negative elongations. There are several demonstrations on how to extract frequencies of the coupling modes from the femtosecond spectra [142–144]. In the present case of fulvene, however, both coupling and tuning modes exhibit oscillations with a period of ~ 20 fs. Hence, we cannot unambiguously obtain information on the coupling modes from the TA PP spectra.

Unfortunately, experimental femtosecond TA PP signals of fulvene are not available. However, the TA PP spectra can be used as important theoretical observables containing useful information on the CI-driven wavepacket dynamics. This is further illustrated by Figure 6 which shows Fourier transforms of the SE (a, c) and ESA (b, d) spectra with respect to the population time τ,

$$I^k_{int}(\Omega, \omega_{pr}) = \int d\tau e^{i\Omega\tau} I^k_{int}(\tau, \omega_{pr}) \tag{28}$$

($k = SE, ESA$). These analyses are inspired by the successful use of beating map for disentangling electronic 2D spectra [145,146]. Let us consider the SE spectrum $I^{SE}_{int}(\Omega, \omega_{pr})$ (a) first. Its value around $\omega_{pr} \sim 4$ eV gives a broad featureless spectrum along Ω which is a mere indication of the short lifetime of the system in S_1. If we move to $\omega_{pr} \sim 2.5$ eV, we see a series of relatively broad peaks which are

Preprints.org (www.preprints.org) | NOT PEER-REVIEWED | Posted: 18 February 2025 doi:10.20944/preprints202502.1269.v1

dominated by the high-intensity peak around $\Omega \approx 1500 - 1700$ cm^{-1}, that yields a 20 fs period which dominates all temporal evolutions of the spectra. The peak widths indicate significance of anharmonic effects produced by nonadiabatic couplings. If we inspect the spectrum around $\omega_{pr} \sim 2.5$ eV, we observe splitting of the majority of the broad peaks into pairs of narrower subpeaks. This is a clear signature of the mode-mode coupling. The ESA spectrum $I_{int}^{ESA}(\Omega, \omega_{pr})$ (b) also reveals multiple broad peaks dominated by the one at $\Omega \approx 1500 - 1700$ cm^{-1}. The peaks do not exhibit the doublet splitting which is characteristic of the SE peaks, owing to the larger number of transitions contributing to the ESA spectra. Exclusion of the first 10 fs from the Fourier transform (panels b, d) removes the most intense part of the TA PP, and the corresponding $I_{int}^{SE}(\Omega, \omega_{pr})$ and $I_{int}^{ESA}(\Omega, \omega_{pr})$ exhibit much simpler peak structures featuring a well separated $\Omega \approx 1500 - 1700$ cm^{-1} peak.

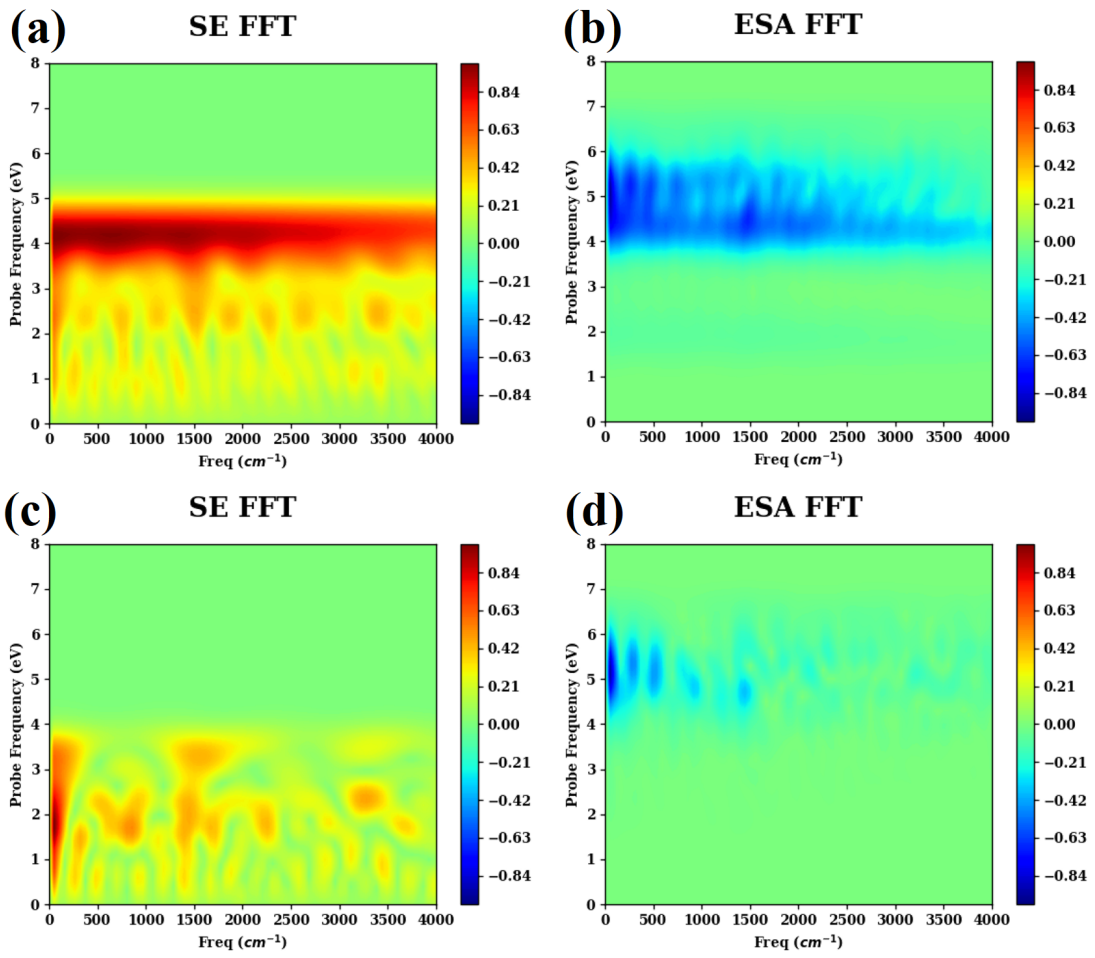

Figure 6. Fourier transforms of the normalized TA PP spectra of fulvene with respect to the population time τ: $I_{int}^{SE}(\Omega, \omega_{pr})$ (a, c) and $I_{int}^{ESA}(\Omega, \omega_{pr})$ (b, d). The upper spectra are computed by integrating from 0 to 600 fs, while the lower spectra are evaluated by integrating from 10 to 600 fs.

4. Conclusions

By combining the SQC/MMST dynamics and the DW representation, we build an efficient protocol for the on-the-fly simulation of femtosecond TA PP signals. The protocol can readily be extended to electronic 2D and other third-order spectroscopic signals.

In the present work, the protocol has been employed to simulate integral TA PP spectrum of fulvene. On the one hand, the SE and ESA contributions to the TA PP spectrum reveal the characteristic times of the CI-driven $S_1 - S_2$ internal conversion which can be extracted from the S_1 population dynamics. On the other hand, analyses of the GSB-cold, GSB-hot, SE, and ESA components of the TA PP spectrum give richer and much more comprehensive information on the nuclear motions contributing to the nonadiabatic dynamics. This indicates that ultrafast spectroscopic signals can

 doi:10.20944/preprints202502.1269.v1

also be considered as information-rich purely theoretical observables, which are complementary to the standard set of dynamic observables which includes evolutions of populations, bond lengths, and bond angles. Taken together, the observables contain information on the peculiarities of the wavepacket motion on the ground and lower-lying excited electronic states, mode-coupling effects, and the leading active modes responsible for the CI-driven $S_1 - S_0$ internal conversion in fulvene. For instance, oscillations of the TA PP signals in the time domain can be attributed to the symmetric stretching and bending modes on the S_1 and S_0 states, and amplitudes of these oscillations provide information on the relative shifts of the corresponding PESs.

Fulvene is a molecular representative of Tully's third model [118]. Recently, Worth and coworkers compared electronic populations of three Tully's molecules predicted by the fewest switches surface hopping method, variational multi-configuration Gaussian (vMCG) method, and (numerically accurate) multi-configuration time-dependent Hartree (MCTDH) method [147]. All calculations employed the linear vibronic coupling (LVC) Hamiltonians developed for the three molecules. As was demonstrated in our work, electronic populations are just the most conventional observables, while much deeper and stringent test would require comparison of nonlinear spectroscopic signals. Obviously, construction of LVC Hamiltonians for higher-lying excited states is a difficult and not fully microscopically justified task, but the available LVC Hamiltonians can be used for the evaluation and comparison of SE and GSB contributions to all third-order spectroscopic signals. The next step may involve testing of on-the-fly and LVC-based signals evaluated by different quantum and quasiclassical methods. Our work can be regarded as a first step in this direction, and the DW methodology can become an efficient tool for the evaluation of all spectroscopic signals.

Author Contributions: Conceptualization, Zhaofa Li, Jiawei Peng, Yifei Zhu, Chao Xu, Maxim F. Gelin, Feng Long Gu and Zhenggang Lan; methodology, Zhaofa Li, Jiawei Peng, Yifei Zhu, Chao Xu, Maxim F. Gelin, Feng Long Gu and Zhenggang Lan; software, Zhaofa Li, Jiawei Peng, Yifei Zhu, Chao Xu, Maxim F. Gelin, Feng Long Gu and Zhenggang Lan; validation, Zhaofa Li, Jiawei Peng, Yifei Zhu, Chao Xu, Maxim F. Gelin, Feng Long Gu and Zhenggang Lan; formal analysis, Zhaofa Li, Jiawei Peng, Yifei Zhu, Chao Xu, Maxim F. Gelin, Feng Long Gu and Zhenggang Lan; investigation, Zhaofa Li, Jiawei Peng, Yifei Zhu, Chao Xu, Maxim F. Gelin, Feng Long Gu and Zhenggang Lan; resources, Zhaofa Li, Jiawei Peng, Yifei Zhu, Chao Xu, Maxim F. Gelin, Feng Long Gu and Zhenggang Lan; data curation, Zhaofa Li, Jiawei Peng, Yifei Zhu, Chao Xu, Maxim F. Gelin, Feng Long Gu and Zhenggang Lan; writing—original draft preparation, Zhaofa Li, Jiawei Peng, Yifei Zhu, Chao Xu, Maxim F. Gelin, Feng Long Gu and Zhenggang Lan; writing—review and editing, Zhaofa Li, Jiawei Peng, Yifei Zhu, Chao Xu, Maxim F. Gelin, Feng Long Gu and Zhenggang Lan; visualization, Zhaofa Li, Jiawei Peng, Yifei Zhu, Chao Xu, Maxim F. Gelin, Feng Long Gu and Zhenggang Lan; supervision, Zhaofa Li, Jiawei Peng, Yifei Zhu, Chao Xu, Maxim F. Gelin, Feng Long Gu and Zhenggang Lan; project administration, Zhaofa Li, Jiawei Peng, Yifei Zhu, Chao Xu, Maxim F. Gelin, Feng Long Gu and Zhenggang Lan; and funding acquisition, Zhaofa Li, Jiawei Peng, Yifei Zhu, Chao Xu, Maxim F. Gelin, Feng Long Gu and Zhenggang Lan. All authors have read and agreed to the published version of the manuscript.

Funding: This work is supported by NSFC projects (No. 22333003, 22361132528, and 21933011). The authors thank the Supercomputing Center, Computer Network Information Center, and Chinese Academy of Sciences. M. F. G. acknowledges support from the National Natural Science Foundation of China (Grant No. 22373028)

Data Availability Statement: The raw data supporting the conclusions of this article will be made available by the authors on request.

Conflicts of Interest: The authors declare no conflicts of interest.

Appendix A

(a) ASSCF(6,6) level are shown in Figure A1.

(b) The long-time TA PP signals are given in Figure A2.

(c) The Fourier transforms of the cold and hot GSB signals are presented in Figure A3.

(d) The evolutions of several additional internal coordinates are displayed in Figure A4.

 doi:10.20944/preprints202502.1269.v1

(e) The excitation energies and TDMs between different electronic states are collected in Table A1.

(f) The normal modes in the states S_0 and S_1 are summarized in Tables A2 and A3, respectively.

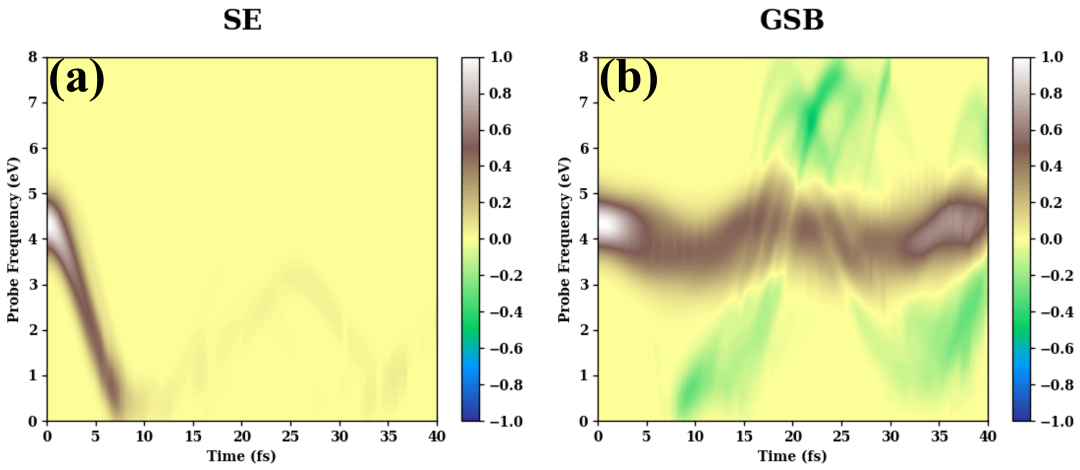

Figure A1. Normalized (a) SE signal, and (b) GSB signal of the fulvene versus the delay time τ and the probe signal ω_{pr} obtained at the SA2-CASSCF(6,6) level of electronic structure theory. The pump-pulse frequency $\omega_{pu} = 4.39$ eV is resonant with the S_1 state.

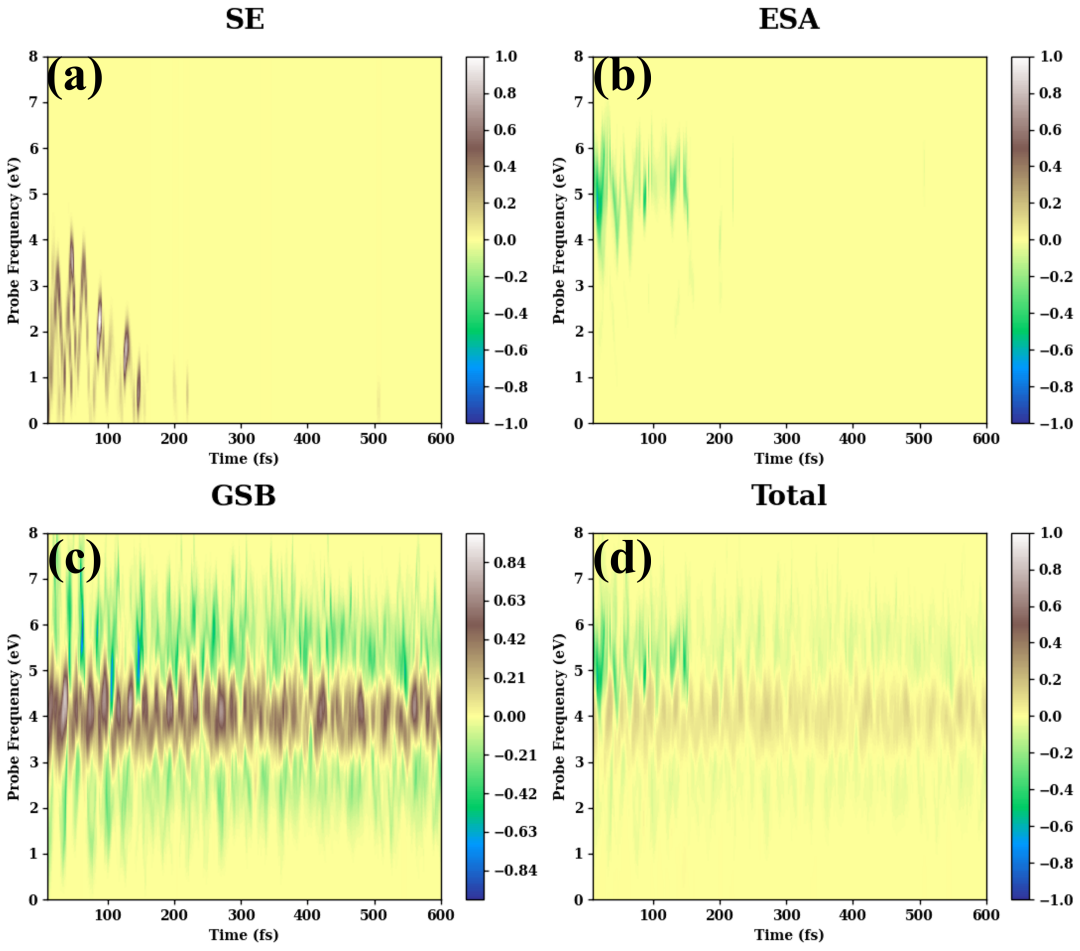

Figure A2. Normalized SE (a), ESA (b), GSB (c) and total (d) integral TA PP spectra of fulvene vs pump-probe delay τ and the probe carrier frequency ω_{pr} evaluated up to 600 fs. The carrier frequency of the pump pulse, $\omega_{pu} = 4.39$ eV is in resonance with the S_1 state.

 doi:10.20944/preprints202502.1269.v1

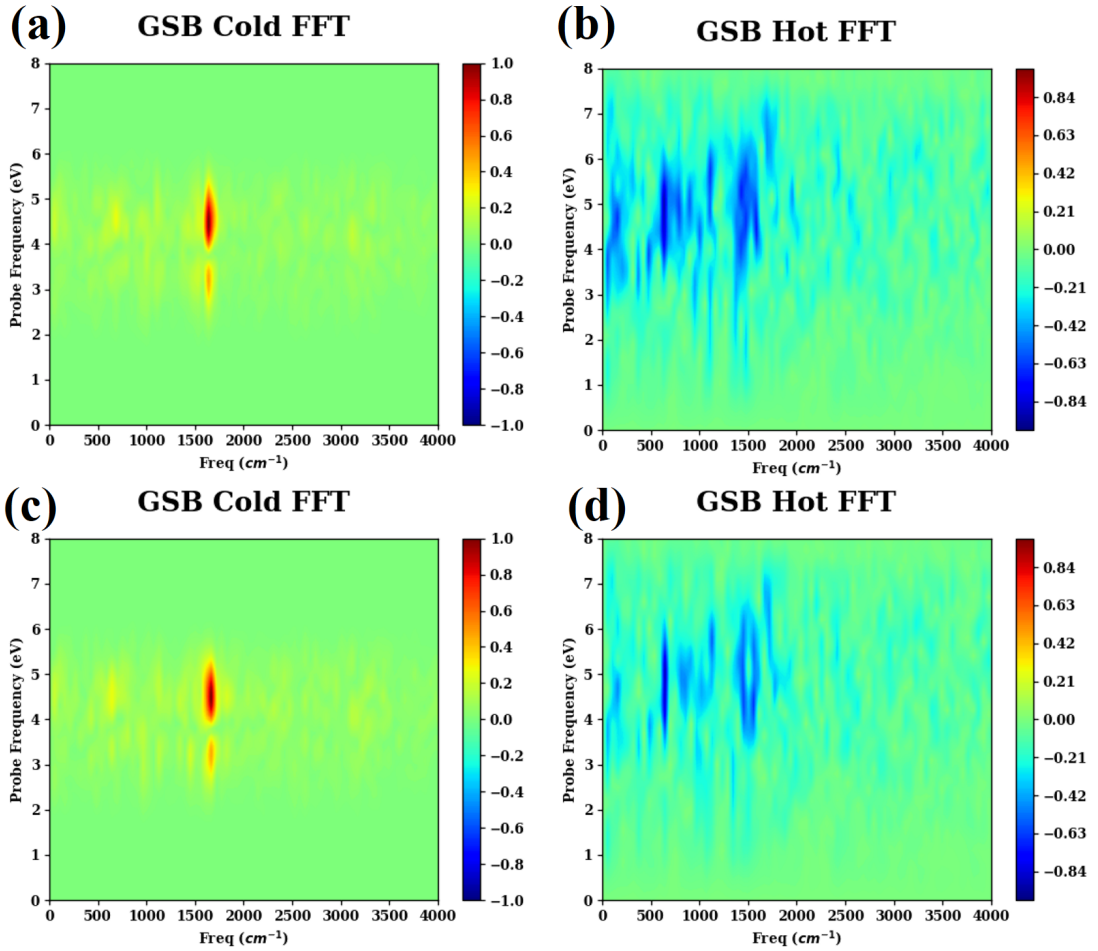

Figure A3. Fourier transforms of the normalized cold (a, c) and hot (b, d) GSB spectra of fulvene. The upper spectra are computed by integrating from 0 to 600 fs, while the lower spectra are evaluated by integrating from 10 to 600 fs.

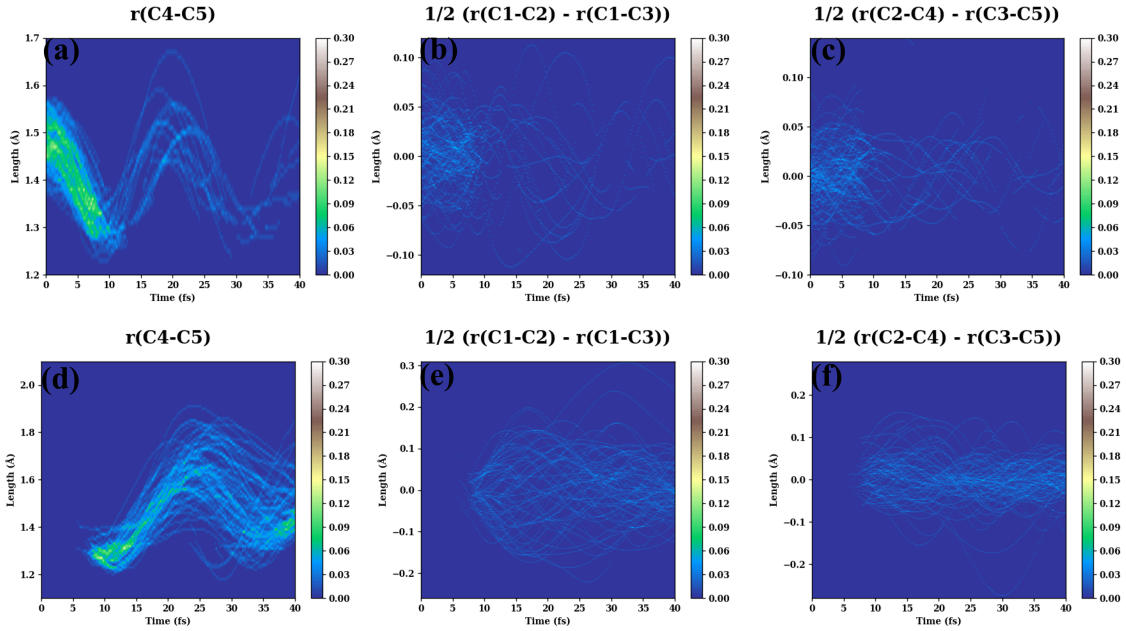

Figure A4. Normalized time-dependent distributions of C4-C5 stretch (a), C1-C2 and C1-C3 asymmetric stretches (b), C2-C4 and C3-C5 asymmetric stretches (c). The upper panels are evaluated for the first excited state S_1, while the lower panels are evaluated for S_0.

 doi:10.20944/preprints202502.1269.v1

Table A1. Energy gaps and TDMs between the selected states of the S_0 minimum at SA6-CASSCF(6,6)/6-31G(d) and the S_0 minimum optimized at SA2-CASSCF(6,6)/6-31G(d).

	Energy gap (eV)	TDM (a.u.)
$S_0 - S_1$	4.39	0.27
$S_1 - S_2$	1.79	0.41
$S_1 - S_3$	3.22	0.21
$S_1 - S_4$	4.03	0.75
$S_1 - S_5$	4.36	0.77

Table A2. Calculated vibrational frequencies of fulvene and their irreducible representations for the S_0 minimum at the SA2-CASSCF(6,6)/6-31G(d) level.

	S_0 frequency cm^{-1} (ranking)	Description
A1	1781.04 (24)	C=C, CH_2 sciss.
	1637.5 (22)	C=C(r) CH_2 sciss.,
	1563.95 (21)	C=C(r), CH_2 sciss., C=C
	1483.03 (20)	CCH, C=C(r), C-C
	1194.15 (17)	CCH
	1048.43 (15)	C-C
	957.18 (13)	C-C
	706.37 (5)	CCC
A2	929.85 (12)	CH wag
	797.32 (8)	CCH_2 tors, CH wag
	715.91 (6)	CCH_2 tors, CH wag
	512.82 (3)	CCCC(r) def
B1	925.66 (11)	CH wag
	906.37 (10)	CH_2 wag
	790.47 (7)	CH wag
	641.15 (4)	CCCC(r) def
	221.89 (1)	CCCC def
B2	1690.56 (23)	C=C(r)
	1461.33 (19)	C=C, CCH
	1368.43 (18)	C=C, CCH
	1187.5 (16)	CCH
	1037.95 (14)	CH_2 rock
	856.37 (9)	CCC(r)
	369.08 (2)	CCC

 doi:10.20944/preprints202502.1269.v1

Table A3. Calculated vibration frequencies of fulvene and their irreducible representations for S_1 minimum at the SA2-CASSCF(6,6)/6-31G(d) level.

	S_0 frequency cm^{-1} (ranking)	S_1 frequency cm^{-1}
A1	1705.61 (23)	C=C, CH_2 sciss.
	1646.85 (22)	C=C(r) CH_2 sciss.,
	1590.15 (21)	C=C(r), CH_2 sciss., C=C
	1326.29 (18)	CCH, C=C(r), C-C
	1210.35 (17)	CCH
	1101.13 (16)	C-C
	1008.5 (14)	C-C
	679.71 (7)	CCC
A2	903.59 (11)	CH wag
	806.51 (10)	CCH_2 tors, CH wag
	549.89 (6)	CCCC(r) def
B1	802.96 (9)	CH wag
	701.58 (8)	CH wag
	532.6 (5)	CCCC(r) def
	270.14 (3)	CCCC def
B2	1873.28 (24)	C=C(r)
	1485.52 (20)	C=C, CCH
	1388.54 (19)	C=C, CCH
	1088.25 (15)	CCH
	996.15 (13)	CH_2 rock
	926.05 (12)	CCC(r)
	322.72 (4)	CCC

References

1. Domcke, W.; Yarkony, D.; Köppel, H. *Conical intersections: electronic structure, dynamics & spectroscopy*; Vol. 15, World Scientific, 2004.
2. Domcke, W.; Yarkony, D.R.; Köppel, H. *Conical intersections: theory, computation and experiment*; Vol. 17, World Scientific, 2011.
3. Yarkony, D.R. Nonadiabatic Quantum Chemistry Past, Present, and Future. *Chemical Reviews* **2012**, *112*, 481–498.
4. Jasper, A.W.; Zhu, C.; Nangia, S.; Truhlar, D.G. Introductory lecture: Nonadiabatic effects in chemical dynamics. *Faraday Discussions* **2004**, *127*, 1–22.
5. Worth, G.A.; Cederbaum, L.S. Beyond Born-Oppenheimer: molecular dynamics through a conical intersection. *Annual Review of Physical Chemistry* **2004**, *55*, 127–158.
6. Schuurman, M.S.; Stolow, A. Dynamics at conical intersections. *Annual Review of Physical Chemistry* **2018**, *69*, 427–450.
7. Matsika, S.; Krause, P. Nonadiabatic events and conical intersections. *Annual Review of Physical Chemistry* **2011**, *62*, 621–643.
8. Domcke, W.; Yarkony, D.R. Role of conical intersections in molecular spectroscopy and photoinduced chemical dynamics. *Annual Review of Physical Chemistry* **2012**, *63*, 325–352.
9. Zewail, A.H. Femtochemistry: Atomic-scale dynamics of the chemical bond. *The Journal of Physical Chemistry A* **2000**, *104*, 5660–5694.
10. Stolow, A. Femtosecond time-resolved photoelectron spectroscopy of polyatomic molecules. *Annual Review of Physical Chemistry* **2003**, *54*, 89–119.
11. Stolow, A.; Bragg, A.E.; Neumark, D.M. Femtosecond time-resolved photoelectron spectroscopy. *Chemical Reviews* **2004**, *104*, 1719–1758.
12. Dietze, D.R.; Mathies, R.A. Femtosecond stimulated Raman spectroscopy. *ChemPhysChem* **2016**, *17*, 1224–1251.
13. Bressler, C.; Chergui, M. Ultrafast X-ray absorption spectroscopy. *Chemical Reviews* **2004**, *104*, 1781–1812.
14. Milne, C.; Penfold, T.; Chergui, M. Recent experimental and theoretical developments in time-resolved X-ray spectroscopies. *Coordination Chemistry Reviews* **2014**, *277*, 44–68.

15. Fushitani, M. Applications of pump-probe spectroscopy. *Annual Reports Section" C"(Physical Chemistry)* **2008**, *104*, 272–297.
16. Ruckebusch, C.; Sliwa, M.; Pernot, P.d.; De Juan, A.; Tauler, R. Comprehensive data analysis of femtosecond transient absorption spectra: A review. *Journal of Photochemistry and Photobiology C: Photochemistry Reviews* **2012**, *13*, 1–27.
17. Braem, O.; Penfold, T.J.; Cannizzo, A.; Chergui, M. A femtosecond fluorescence study of vibrational relaxation and cooling dynamics of UV dyes. *Physical Chemistry Chemical Physics* **2012**, *14*, 3513–3519.
18. Hall, G.E.; North, S.W. Transient laser frequency modulation spectroscopy. *Annual Review of Physical Chemistry* **2000**, *51*, 243–274.
19. Crespo-Hernández, C.E.; Cohen, B.; Hare, P.M.; Kohler, B. Ultrafast excited-state dynamics in nucleic acids. *Chemical Reviews* **2004**, *104*, 1977–2020.
20. Rulliere, C.; et al. *Femtosecond laser pulses*; Springer, 2005.
21. Diels, J.C.; Rudolph, W. *Ultrashort laser pulse phenomena*; Elsevier, 2006.
22. Wei, Z.; Nakamura, T.; Takeuchi, S.; Tahara, T. Tracking of the nuclear wavepacket motion in cyanine photoisomerization by ultrafast pump–dump–probe spectroscopy. *Journal of the American Chemical Society* **2011**, *133*, 8205–8210.
23. Auböck, G.; Consani, C.; van Mourik, F.; Chergui, M. Ultrabroadband femtosecond two-dimensional ultraviolet transient absorption. *Optics Letters* **2012**, *37*, 2337–2339.
24. Davydova, D.; de la Cadena, A.; Akimov, D.; Dietzek, B. Transient absorption microscopy: advances in chemical imaging of photoinduced dynamics. *Laser & Photonics Reviews* **2016**, *10*, 62–81.
25. Mukamel, S. *Principles of Nonlinear Optical Spectroscopy*; Oxford series in optical and imaging sciences, Oxford University Press, 1995.
26. Egorova, D. Detection of electronic and vibrational coherences in molecular systems by 2D electronic photon echo spectroscopy. *Chemical Physics* **2008**, *347*, 166–176.
27. Kowalewski, M.; Bennett, K.; Dorfman, K.E.; Mukamel, S. Catching conical intersections in the act: Monitoring transient electronic coherences by attosecond stimulated X-ray Raman signals. *Physical Review Letters* **2015**, *115*, 193003.
28. Kowalewski, M.; Bennett, K.; Mukamel, S. Monitoring nonadiabatic avoided crossing dynamics in molecules by ultrafast X-ray diffraction. *Structural Dynamics* **2017**, *4*, 054101.
29. Bennett, K.; Kowalewski, M.; Rouxel, J.R.; Mukamel, S. Monitoring molecular nonadiabatic dynamics with femtosecond X-ray diffraction. *Proceedings of the National Academy of Sciences* **2018**, *115*, 6538–6547.
30. Segatta, F.; Nenov, A.; Orlandi, S.; Arcioni, A.; Mukamel, S.; Garavelli, M. Exploring the capabilities of optical pump X-ray probe NEXAFS spectroscopy to track photo-induced dynamics mediated by conical intersections. *Faraday Discussions* **2020**, *221*, 245–264.
31. Liu, Y.; Martínez-Fernández, L.; Cerezo, J.; Prampolini, G.; Improta, R.; Santoro, F. Multistate coupled quantum dynamics of photoexcited cytosine in gas-phase: Nonadiabatic absorption spectrum and ultrafast internal conversions. *Chemical Physics* **2018**, *515*, 452–463.
32. Wang, H.; Thoss, M. Nonperturbative quantum simulation of time-resolved nonlinear spectra: Methodology and application to electron transfer reactions in the condensed phase. *Chemical Physics* **2008**, *347*, 139–151.
33. Kramer, T.; Noack, M.; Reinefeld, A.; Rodríguez, M.; Zelinskyy, Y. Efficient calculation of open quantum system dynamics and time-resolved spectroscopy with distributed memory HEOM (DM-HEOM). *Journal of Computational Chemistry* **2018**, *39*, 1779–1794.
34. Toutounji, M. Electronic dephasing of polyatomic molecules interacting with mixed quantum-classical media. *Physical Chemistry Chemical Physics* **2021**, *23*, 21981–21994.
35. Toutounji, M. Mixed Quantum-Classical Liouville Equation Treatment of Electronic Spectroscopy of Condensed Systems: Harmonic and Anharmonic Electron–Phonon Coupling. *Journal of Chemical Theory and Computation* **2023**, *19*, 3779–3797.
36. Petit, A.S.; Subotnik, J.E. Calculating time-resolved differential absorbance spectra for ultrafast pump-probe experiments with surface hopping trajectories. *The Journal of Chemical Physics* **2014**, *141*.
37. Petit, A.S.; Subotnik, J.E. How to calculate linear absorption spectra with lifetime broadening using fewest switches surface hopping trajectories: A simple generalization of ground-state Kubo theory. *The Journal of Chemical Physics* **2014**, *141*, 014107.
38. Tempelaar, R.; Van Der Vegte, C.P.; Knoester, J.; Jansen, T.L. Surface hopping modeling of two-dimensional spectra. *The Journal of Chemical Physics* **2013**, *138*, 164106.

39. Humeniuk, A.; Wohlgemuth, M.; Suzuki, T.; Mitrić, R. Time-resolved photoelectron imaging spectra from non-adiabatic molecular dynamics simulations. *The Journal of Chemical Physics* **2013**, *139*, 134104.
40. Van Der Vegte, C.; Dijkstra, A.; Knoester, J.; Jansen, T. Calculating two-dimensional spectra with the mixed quantum-classical ehrenfest method. *The Journal of Physical Chemistry A* **2013**, *117*, 5970–5980.
41. Heller, E.J. *The semiclassical way to dynamics and spectroscopy*; Princeton University Press, 2018.
42. Kowalewski, M.; Fingerhut, B.P.; Dorfman, K.E.; Bennett, K.; Mukamel, S. Simulating coherent multidimensional spectroscopy of nonadiabatic molecular processes: From the infrared to the x-ray regime. *Chemical Reviews* **2017**, *117*, 12165–12226.
43. Crespo-Otero, R.; Barbatti, M. Recent advances and perspectives on nonadiabatic mixed quantum–classical dynamics. *Chemical Reviews* **2018**, *118*, 7026–7068.
44. Mai, S.; González, L. Molecular photochemistry: recent developments in theory. *Angewandte Chemie International Edition* **2020**, *59*, 16832–16846.
45. Conti, I.; Cerullo, G.; Nenov, A.; Garavelli, M. Ultrafast spectroscopy of photoactive molecular systems from first principles: Where we stand today and where we are going. *Journal of the American Chemical Society* **2020**, *142*, 16117–16139.
46. Loring, R.F. Calculating multidimensional optical spectra from classical trajectories. *Annual Review of Physical Chemistry* **2022**, *73*, 273–297.
47. Yan, Y.; Liu, Y.; Xing, T.; Shi, Q. Theoretical Study of Excitation Energy Transfer and Nonlinear Spectroscopy of Photosynthetic Light- Harvesting Complexes Using the Nonperturbative Reduced Dynamics Method. *WIREs Computational Molecular Science* **2021**, *11*, e1498.
48. Gelin, M.F.; Chen, L.; Domcke, W. Equation-of-motion methods for the calculation of femtosecond time-resolved 4-wave-mixing and N-wave-mixing signals. *Chemical Reviews* **2022**, *122*, 17339–17396.
49. Jansen, T.L.C. Computational spectroscopy of complex systems. *The Journal of Chemical Physics* **2021**, *155*, 170901.
50. Krumland, J.; Guerrini, M.; De Sio, A.; Lienau, C.; Cocchi, C. Two-dimensional electronic spectroscopy from first principles. *Applied Physics Reviews* **2024**, *11*, 011305.
51. Faraji, S.; Picconi, D.; Palacino-González, E. Advanced quantum and semiclassical methods for simulating photoinduced molecular dynamics and spectroscopy. *WIREs Computational Molecular Science* **2024**, *14*, e1731.
52. Richter, M.; Fingerhut, B.P. Simulation of multi-dimensional signals in the optical domain: Quantum-classical feedback in nonlinear exciton propagation. *Journal of Chemical Theory and Computation* **2016**, *12*, 3284–3294.
53. Šulc, M.; Hernández, H.; Martínez, T.J.; Vaníček, J. Relation of exact Gaussian basis methods to the dephasing representation: Theory and application to time-resolved electronic spectra. *The Journal of Chemical Physics* **2013**, *139*, 034112.
54. Zimmermann, T.; Vaníček, J. Efficient on-the-fly ab initio semiclassical method for computing time-resolved nonadiabatic electronic spectra with surface hopping or Ehrenfest dynamics. *The Journal of Chemical Physics* **2014**, *141*, 134102.
55. Begušić, T.; Roulet, J.; Vaníček, J. On-the-fly ab initio semiclassical evaluation of time-resolved electronic spectra. *The Journal of Chemical Physics* **2018**, *149*, 244115.
56. Begušić, T.; Vaníček, J. On-the-fly ab initio semiclassical evaluation of third-order response functions for two-dimensional electronic spectroscopy. *The Journal of Chemical Physics* **2020**, *153*, 184110.
57. Nguyen, T.S.; Koh, J.H.; Lefelhocz, S.; Parkhill, J. Black-box, real-time simulations of transient absorption spectroscopy. *The Journal of Physical Chemistry Letters* **2016**, *7*, 1590–1595.
58. Meyer, H.D.; Miller, W.H. A classical analog for electronic degrees of freedom in nonadiabatic collision processes. *The Journal of Chemical Physics* **1979**, *70*, 3214–3223.
59. Stock, G.; Thoss, M. Semiclassical description of nonadiabatic quantum dynamics. *Physical Review Letters* **1997**, *78*, 578.
60. Thoss, M.; Stock, G. Mapping approach to the semiclassical description of nonadiabatic quantum dynamics. *Physical Review A* **1999**, *59*, 64.
61. Huo, P.; Coker, D.F. Communication: Partial linearized density matrix dynamics for dissipative, non-adiabatic quantum evolution. *The Journal of Chemical Physics* **2011**, *135*, 201101.
62. Lee, M.K.; Huo, P.; Coker, D.F. Semiclassical path integral dynamics: Photosynthetic energy transfer with realistic environment interactions. *Annual Review of Physical Chemistry* **2016**, *67*, 639–668.
63. Hsieh, C.Y.; Schofield, J.; Kapral, R. Forward–backward solution of quantum-classical Liouville equation in the adiabatic mapping basis. *Molecular Physics* **2013**, *111*, 3546–3554.

 doi:10.20944/preprints202502.1269.v1

64. Liu, J.; He, X.; Wu, B. Unified formulation of phase space mapping approaches for nonadiabatic quantum dynamics. *Accounts of Chemical Research* **2021**, *54*, 4215–4228.
65. He, X.; Wu, B.; Shang, Y.; Li, B.; Cheng, X.; Liu, J. New phase space formulations and quantum dynamics approaches. *Wiley Interdisciplinary Reviews: Computational Molecular Science* **2022**, *12*, e1619.
66. Wu, B.; He, X.; Liu, J. Nonadiabatic Field on Quantum Phase Space: A Century after Ehrenfest. *The Journal of Physical Chemistry Letters* **2024**, *15*, 644–658.
67. Miller, W.H.; Cotton, S.J. Classical molecular dynamics simulation of electronically non-adiabatic processes. *Faraday Discussions* **2016**, *195*, 9–30.
68. Mandal, A.; Yamijala, S.S.; Huo, P. Quasi-diabatic representation for nonadiabatic dynamics propagation. *Journal of Chemical Theory and Computation* **2018**, *14*, 1828–1840.
69. Zhou, W.; Mandal, A.; Huo, P. Quasi-diabatic scheme for nonadiabatic on-the-fly simulations. *The Journal of Physical Chemistry Letters* **2019**, *10*, 7062–7070.
70. Hu, D.; Mandal, A.; Weight, B.M.; Huo, P. Quasi-diabatic propagation scheme for simulating polariton chemistry. *The Journal of Chemical Physics* **2022**, *157*, 194109.
71. Church, M.S.; Hele, T.J.; Ezra, G.S.; Ananth, N. Nonadiabatic semiclassical dynamics in the mixed quantum-classical initial value representation. *The Journal of Chemical Physics* **2018**, *148*, 102326.
72. Conte, R.; Aieta, C.; Cazzaniga, M.; Ceotto, M. A perspective on the investigation of spectroscopy and kinetics of complex molecular systems with semiclassical approaches. *The Journal of Physical Chemistry Letters* **2024**, *15*, 7566–7576.
73. Stock, G.; Miller, W.H. A classical model for time-and frequency-resolved spectroscopy of nonadiabatic excited-state dynamics. *Chemical Physics Letters* **1992**, *197*, 396–404.
74. Uspenskiy, I.; Strodel, B.; Stock, G. Classical calculation of transient absorption spectra monitoring ultrafast electron transfer processes. *Journal of Chemical Theory and Computation* **2006**, *2*, 1605–1617.
75. Uspenskiy, I.; Strodel, B.; Stock, G. Classical description of the dynamics and time-resolved spectroscopy of nonadiabatic cis–trans photoisomerization. *Chemical Physics* **2006**, *329*, 109–117.
76. Loring, R.F. Mean-trajectory approximation for electronic and vibrational-electronic nonlinear spectroscopy. *The Journal of Chemical Physics* **2017**, *146*, 144106.
77. Polley, K.; Loring, R.F. Two-dimensional vibronic spectra from classical trajectories. *The Journal of Chemical Physics* **2019**, *150*, 164114.
78. Kwac, K.; Geva, E. A mixed quantum-classical molecular dynamics study of the hydroxyl stretch in methanol/carbon tetrachloride mixtures III: Nonequilibrium hydrogen-bond dynamics and infrared pump–probe spectra. *The Journal of Physical Chemistry B* **2013**, *117*, 7737–7749.
79. Gao, X.; Lai, Y.; Geva, E. Simulating absorption spectra of multiexcitonic systems via quasiclassical mapping Hamiltonian methods. *Journal of Chemical Theory and Computation* **2020**, *16*, 6465–6480.
80. Gao, X.; Geva, E. A nonperturbative methodology for simulating multidimensional spectra of multiexcitonic molecular systems via quasiclassical mapping Hamiltonian methods. *Journal of Chemical Theory and Computation* **2020**, *16*, 6491–6502.
81. McRobbie, P.L.; Hanna, G.; Shi, Q.; Geva, E. Signatures of nonequilibrium solvation dynamics on multidimensional spectra. *Accounts of Chemical Research* **2009**, *42*, 1299–1309.
82. Bai, S.; Xie, W.; Zhu, L.; Shi, Q. Calculation of absorption spectra involving multiple excited states: Approximate methods based on the mixed quantum classical Liouville equation. *The Journal of Chemical Physics* **2014**, *140*, 084105.
83. Provazza, J.; Segatta, F.; Garavelli, M.; Coker, D.F. Semiclassical path integral calculation of nonlinear optical spectroscopy. *Journal of Chemical Theory and Computation* **2018**, *14*, 856–866.
84. Provazza, J.; Coker, D.F. Communication: Symmetrical quasi-classical analysis of linear optical spectroscopy. *The Journal of Chemical Physics* **2018**, *148*, 181102.
85. Provazza, J.; Segatta, F.; Coker, D.F. Modeling nonperturbative field-driven vibronic dynamics: Selective state preparation and nonlinear spectroscopy. *Journal of Chemical Theory and Computation* **2020**, *17*, 29–39.
86. Sun, X. Hybrid equilibrium-nonequilibrium molecular dynamics approach for two-dimensional solute-pump/solvent-probe spectroscopy. *The Journal of Chemical Physics* **2019**, *151*, 194507.
87. Karsten, S.; Ivanov, S.D.; Bokarev, S.I.; Kühn, O. Quasi-classical approaches to vibronic spectra revisited. *The Journal of Chemical Physics* **2018**, *148*, 102337.
88. Mannouch, J.R.; Richardson, J.O. A partially linearized spin-mapping approach for simulating nonlinear optical spectra. *The Journal of Chemical Physics* **2022**, *156*, 024108.

89. Polley, K.; Loring, R.F. Spectroscopic response theory with classical mapping Hamiltonians. *The Journal of Chemical Physics* **2020**, *153*, 204103.
90. Seidner, L.; Stock, G.; Domcke, W. Nonperturbative approach to femtosecond spectroscopy: General theory and application to multidimensional nonadiabatic photoisomerization processes. *The Journal of Chemical Physics* **1995**, *103*, 3998–4011.
91. Gelin, M.F.; Egorova, D.; Domcke, W. Efficient method for the calculation of time-and frequency-resolved four-wave mixing signals and its application to photon-echo spectroscopy. *The Journal of Chemical Physics* **2005**, *123*, 164112.
92. Mančal, T.; Pisliakov, A.V.; Fleming, G.R. Two-dimensional optical three-pulse photon echo spectroscopy. I. Nonperturbative approach to the calculation of spectra. *The Journal of Chemical Physics* **2006**, *124*, 234504.
93. Ka, B.J.; Geva, E. A nonperturbative calculation of nonlinear spectroscopic signals in liquid solution. *The Journal of Chemical Physics* **2006**, *125*, 214501.
94. Yan, Y.J.; Fried, L.E.; Mukamel, S. Ultrafast pump-probe spectroscopy: femtosecond dynamics in Liouville space. *The Journal of Physical Chemistry* **1989**, *93*, 8149–8162.
95. Yan, Y.J.; Mukamel, S. Femtosecond pump-probe spectroscopy of polyatomic molecules in condensed phases. *Physical Review A* **1990**, *41*, 6485.
96. Bosma, W.B.; Yan, Y.J.; Mukamel, S. Intramolecular and solvent dynamics in femtosecond pump–probe spectroscopy. *The Journal of Chemical Physics* **1990**, *93*, 3863–3873.
97. Pollard, W.T.; Lee, S.Y.; Mathies, R.A. Wave packet theory of dynamic absorption spectra in femtosecond pump–probe experiments. *The Journal of Chemical Physics* **1990**, *92*, 4012–4029.
98. Pollard, W.T.; Mathies, R.A. Analysis of femtosecond dynamic absorption spectra of nonstationary states. *Annual Review of Physical Chemistry* **1992**, *43*, 497–523.
99. Xu, C.; Lin, C.; Peng, J.; Zhang, J.; Lin, S.; Gu, F.L.; Gelin, M.F.; Lan, Z. On-the-fly simulation of time-resolved fluorescence spectra and anisotropy. *The Journal of Chemical Physics* **2024**, *160*, 104109.
100. Xu, C.; Lin, K.; Hu, D.; Gu, F.L.; Gelin, M.F.; Lan, Z. Ultrafast internal conversion dynamics through the on-the-Fly simulation of transient absorption pump–probe spectra with different electronic structure methods. *The Journal of Physical Chemistry Letters* **2022**, *13*, 661–668.
101. Hu, D.; Peng, J.; Chen, L.; Gelin, M.F.; Lan, Z. Spectral fingerprint of excited-state energy transfer in dendrimers through polarization-sensitive transient-absorption pump–probe signals: On-the-fly nonadiabatic dynamics simulations. *The Journal of Physical Chemistry Letters* **2021**, *12*, 9710–9719.
102. Gelin, M.F.; Huang, X.; Xie, W.; Chen, L.; Došlić, N.; Domcke, W. Ab initio surface-hopping simulation of femtosecond transient-absorption pump–probe signals of nonadiabatic excited-state dynamics using the doorway–window representation. *Journal of Chemical Theory and Computation* **2021**, *17*, 2394–2408.
103. Huang, X.; Xie, W.; Došlić, N.; Gelin, M.F.; Domcke, W. Ab initio quasiclassical simulation of femtosecond time-resolved two-dimensional electronic spectra of pyrazine. *The Journal of Physical Chemistry Letters* **2021**, *12*, 11736–11744.
104. Pios, S.V.; Gelin, M.F.; Ullah, A.; Dral, P.O.; Chen, L. Artificial-Intelligence-Enhanced On-the-Fly Simulation of Nonlinear Time-Resolved Spectra. *The Journal of Physical Chemistry Letters* **2024**, *15*, 2325–2331.
105. Perez-Castillo, R.; Freixas, V.M.; Mukamel, S.; Martinez-Mesa, A.; Uranga-Pina, L.; Tretiak, S.; Gelin, M.F.; Fernandez-Alberti, S. Transient-absorption spectroscopy of dendrimers via nonadiabatic excited-state dynamics simulations. *Chemical Science* **2024**, *15*, 13250–13261. https://doi.org/10.1039/D4SC01019A.
106. Li, Z.; Peng, J.; Zhu, Y.; Xu, C.; Gelin, M.F.; Gu, F.L.; Lan, Z. On-the-fly simulations of transient absorption pump-probe spectra: combining mapping dynamics with doorway-window protocol **2024**.
107. Cotton, S.J.; Miller, W.H. Symmetrical windowing for quantum states in quasi-classical trajectory simulations. *The Journal of Physical Chemistry A* **2013**, *117*, 7190–7194.
108. Cotton, S.J.; Miller, W.H. Symmetrical windowing for quantum states in quasi-classical trajectory simulations: Application to electronically non-adiabatic processes. *The Journal of Chemical Physics* **2013**, *139*, 234112.
109. Xie, Y.; Zheng, J.; Lan, Z. Performance evaluation of the symmetrical quasi-classical dynamics method based on Meyer-Miller mapping Hamiltonian in the treatment of site-exciton models. *The Journal of Chemical Physics* **2018**, *149*, 174105.
110. He, X.; Cheng, X.; Wu, B.; Liu, J. Nonadiabatic Field with Triangle Window Functions on Quantum Phase Space. *The Journal of Physical Chemistry Letters* **2024**, *15*, 5452–5466.
111. Gao, X.; Saller, M.A.; Liu, Y.; Kelly, A.; Richardson, J.O.; Geva, E. Benchmarking quasiclassical mapping Hamiltonian methods for simulating electronically nonadiabatic molecular dynamics. *Journal of Chemical Theory and Computation* **2020**, *16*, 2883–2895.

 doi:10.20944/preprints202502.1269.v1

112. Jain, A.; Subotnik, J.E. Vibrational energy relaxation: A benchmark for mixed quantum–classical methods. *The Journal of Physical Chemistry A* **2018**, *122*, 16–27.
113. Stock, G.; Thoss, M. Classical description of nonadiabatic quantum dynamics. *Advances in Chemical Physics* **2005**, *131*, 243–375.
114. Cotton, S.J.; Liang, R.; Miller, W.H. On the adiabatic representation of Meyer-Miller electronic-nuclear dynamics. *The Journal of Chemical Physics* **2017**, *147*, 064112.
115. Tang, D.; Fang, W.H.; Shen, L.; Cui, G. Combining Meyer–Miller Hamiltonian with electronic structure methods for on-the-fly nonadiabatic dynamics simulations: implementation and application. *Physical Chemistry Chemical Physics* **2019**, *21*, 17109–17117.
116. Hu, D.; Xie, Y.; Peng, J.; Lan, Z. On-the-fly symmetrical quasi-classical dynamics with Meyer–Miller mapping Hamiltonian for the treatment of nonadiabatic dynamics at conical intersections. *Journal of Chemical Theory and Computation* **2021**, *17*, 3267–3279.
117. Talbot, J.J.; Head-Gordon, M.; Cotton, S.J. The symmetric quasi-classical model using on-the-fly time-dependent density functional theory within the Tamm–Dancoff approximation. *Molecular Physics* **2023**, *121*, e2153761.
118. Tully, J.C. Molecular dynamics with electronic transitions. *The Journal of Chemical Physics* **1990**, *93*, 1061–1071.
119. Ibele, L.M.; Curchod, B.F. A molecular perspective on Tully models for nonadiabatic dynamics. *Physical Chemistry Chemical Physics* **2020**, *22*, 15183–15196.
120. Ibele, L.M.; Lassmann, Y.; Martínez, T.J.; Curchod, B.F. Comparing (stochastic-selection) ab initio multiple spawning with trajectory surface hopping for the photodynamics of cyclopropanone, fulvene, and dithiane. *The Journal of Chemical Physics* **2021**, *154*, 104110.
121. Vindel-Zandbergen, P.; Ibele, L.M.; Ha, J.K.; Min, S.K.; Curchod, B.F.; Maitra, N.T. Study of the decoherence correction derived from the exact factorization approach for nonadiabatic dynamics. *Journal of Chemical Theory and Computation* **2021**, *17*, 3852–3862.
122. Weight, B.M.; Mandal, A.; Huo, P. Ab initio symmetric quasi-classical approach to investigate molecular Tully models. *The Journal of Chemical Physics* **2021**, *155*, 084106.
123. Grohmann, T.; Deeb, O.; Leibscher, M. Quantum separation of para-and ortho-fulvene with coherent light: The influence of the conical intersection. *Chemical Physics* **2007**, *338*, 252–258.
124. Alfalah, S.; Belz, S.; Deeb, O.; Leibscher, M.; Manz, J.; Zilberg, S. Photoinduced quantum dynamics of ortho-and para-fulvene: Hindered photoisomerization due to mode selective fast radiationless decay via a conical intersection. *The Journal of Chemical Physics* **2009**, *130*, 124318.
125. Mendive-Tapia, D.; Lasorne, B.; Worth, G.A.; Bearpark, M.J.; Robb, M.A. Controlling the mechanism of fulvene S 1/S 0 decay: switching off the stepwise population transfer. *Physical Chemistry Chemical Physics* **2010**, *12*, 15725–15733.
126. Mendive-Tapia, D.; Lasorne, B.; Worth, G.A.; Robb, M.A.; Bearpark, M.J. Towards converging non-adiabatic direct dynamics calculations using frozen-width variational Gaussian product basis functions. *The Journal of Chemical Physics* **2012**, *137*, 22A548.
127. Bearpark, M.J.; Bernardi, F.; Olivucci, M.; Robb, M.A.; Smith, B.R. Can fulvene S1 decay be controlled? A CASSCF study with MMVB dynamics. *Journal of the American Chemical Society* **1996**, *118*, 5254–5260.
128. Toldo, J.M.; Mattos, R.S.; Pinheiro Jr, M.; Mukherjee, S.; Barbatti, M. Recommendations for velocity adjustment in surface hopping. *Journal of Chemical Theory and Computation* **2024**, *20*, 614–624.
129. Cotton, S.J.; Miller, W.H. A new symmetrical quasi-classical model for electronically non-adiabatic processes: Application to the case of weak non-adiabatic coupling. *The Journal of Chemical Physics* **2016**, *145*, 144108.
130. Cotton, S.J.; Miller, W.H. A symmetrical quasi-classical windowing model for the molecular dynamics treatment of non-adiabatic processes involving many electronic states. *The Journal of Chemical Physics* **2019**, *150*, 104101.
131. Liu, J. A unified theoretical framework for mapping models for the multi-state Hamiltonian. *The Journal of Chemical Physics* **2016**, *145*, 204105.
132. Cheng, X.; He, X.; Liu, J. A novel class of phase space representations for the exact population dynamics of two-state quantum systems and the relation to triangle window functions. *Chinese Journal of Chemical Physics* **2024**, *37*, 230–254.
133. Gao, X.; Geva, E. Improving the accuracy of quasiclassical mapping Hamiltonian methods by treating the window function width as an adjustable parameter. *The Journal of Physical Chemistry A* **2020**, *124*, 11006–11016.

134. Cotton, S.J.; Miller, W.H. Trajectory-adjusted electronic zero point energy in classical Meyer-Miller vibronic dynamics: Symmetrical quasiclassical application to photodissociation. *The Journal of Chemical Physics* **2019**, *150*, 194110.
135. He, X.; Gong, Z.; Wu, B.; Liu, J. Negative zero-point-energy parameter in the Meyer–Miller mapping model for nonadiabatic dynamics. *The Journal of Physical Chemistry Letters* **2021**, *12*, 2496–2501.
136. He, X.; Wu, B.; Gong, Z.; Liu, J. Commutator matrix in phase space mapping models for nonadiabatic quantum dynamics. *The Journal of Physical Chemistry A* **2021**, *125*, 6845–6863.
137. Lax, M. The Franck-Condon principle and its application to crystals. *Journal of Chemical Physics* **1952**, *20*, 1752–1760.
138. Hillery, M.; O'Connel, R.F.; Scully, M.O.; Wigner, E.P. Distribution Functions in Physics: Fundamentals. *Phys. Rep.* **1984**, *106*, 121–167.
139. Frisch, M.J.; Trucks, G.W.; Schlegel, H.B.; Scuseria, G.E.; Robb, M.A.; Cheeseman, J.R.; Scalmani, G.; Barone, V.; Petersson, G.A.; Nakatsuji, H.; et al. Gaussian~16 Revision C.01, 2016. Gaussian Inc. Wallingford CT.
140. Werner, H.J.; Knowles, P.J.; Manby, F.R.; Black, J.A.; Doll, K.; Heßelmann, A.; Kats, D.; Köhn, A.; Korona, T.; Kreplin, D.A.; et al. The Molpro quantum chemistry package. *The Journal of Chemical Physics* **2020**, *152*, 144107.
141. Du, L.; Lan, Z. An on-the-fly surface-hopping program jade for nonadiabatic molecular dynamics of polyatomic systems: implementation and applications. *Journal of Chemical Theory and Computation* **2015**, *11*, 1360–1374.
142. Farag, M.H.; Jansen, T.L.; Knoester, J. Probing the interstate coupling near a conical intersection by optical spectroscopy. *The Journal of Physical Chemistry Letters* **2016**, *7*, 3328–3334.
143. Zhan, S.; Gelin, M.F.; Huang, X.; Sun, K. Ab initio simulation of peak evolutions and beating maps for electronic two-dimensional signals of a polyatomic chromophore. *Journal of Chemical Physics* **2023**, *158*, 194106.
144. Qiang, Y.; Sun, K.; Palacino-González, E.; Shen, K.; Rao, B.J.; Gelin, M.F.; Zhao, Y. Probing avoided crossings and conical intersections by two-pulse femtosecond stimulated Raman spectroscopy: Theoretical study. *Journal of Chemical Physics* **2024**, *160*, 054107.
145. Butkus, V.; Zigmantas, D.; Valkunas, L.; Abramavicius, D. Vibrational vs. Electronic coherences in 2D spectrum of molecular systems. *Chemical Physics Letters* **2012**, *545*, 40–43.
146. Butkus, V.; Valkunas, L.; Abramavicius, D. Molecular vibrations-induced quantum beats in two-dimensional electronic spectroscopy. *Journal of Chemical Physics* **2012**, *137*, 044513.
147. Gómez, S.; Spinlove, E.; Worth, G. Benchmarking non-adiabatic quantum dynamics using the molecular Tully models. *Physical Chemistry Chemical Physics* **2024**, *26*, 1829–1844.